Chapter 4

Magnetic confinement of winds

Science is experiment; science is trying things.
It is trying each possible alternative in turn,
intelligently and systematically;
and throwing away what won't work, and accepting what will,
no matter how it goes against our prejudices.

Jacob Bronowski
A Sense of the Future (1948)

4.1 Magnetic fields in the solar corona

Up to now we have considered the dynamics of the coronal plasma independently of the coronal magnetic field, which we had earlier argued (§3.1.1) is a dominant structural agent in the corona. In this chapter we begin to flirt with the interaction of magnetic fields and plasma flow, by considering its two limiting cases, when either the plasma or magnetic field entirely dominates the force balance. Once again we stick mostly to the sun as our exemplar of magnetic confinement of stellar winds in general.

The interaction between the coronal plasma and magnetic field owes a lot of its complexity to the fact that the two are tightly coupled under typical coronal conditions. A central concept is that of **flux-freezing**, already encountered in §1.10; in a highly conducting plasma in a steady-state, plasma can only flow along magnetic fieldlines, i.e., $\mathbf{u} \times \mathbf{B} = 0$. The induction equation (in the $\eta \to 0$ limit, as per the high electrical conductivity) then yields $\partial \mathbf{B}/\partial t = 0$, which of course is precisely what is required for a steady-state to be maintained.

You may recall (chap. 1) that the magnetic Reynolds number (eq. (1.63) in the corona is gigantic, i.e., $\sim 10^{12}$. This is not so much because the coronal plasma is such a good electrical conductor (pure copper at room temperature is a hundred times better!), but because the flow speeds in the corona are relatively high, and the dimensions involved, of order R, are so large. Consequently, care must be exercised when applying the flux-freezing approximation in modelling structures evolving on small spatial scales, but on the large scales it is usually a very good approximation.

4.2 The plasma-β

We must first ask under which circumstances the coronal dynamics is dominated by either the plasma or magnetic field. This is far from a trivial question. A useful quantity, called the

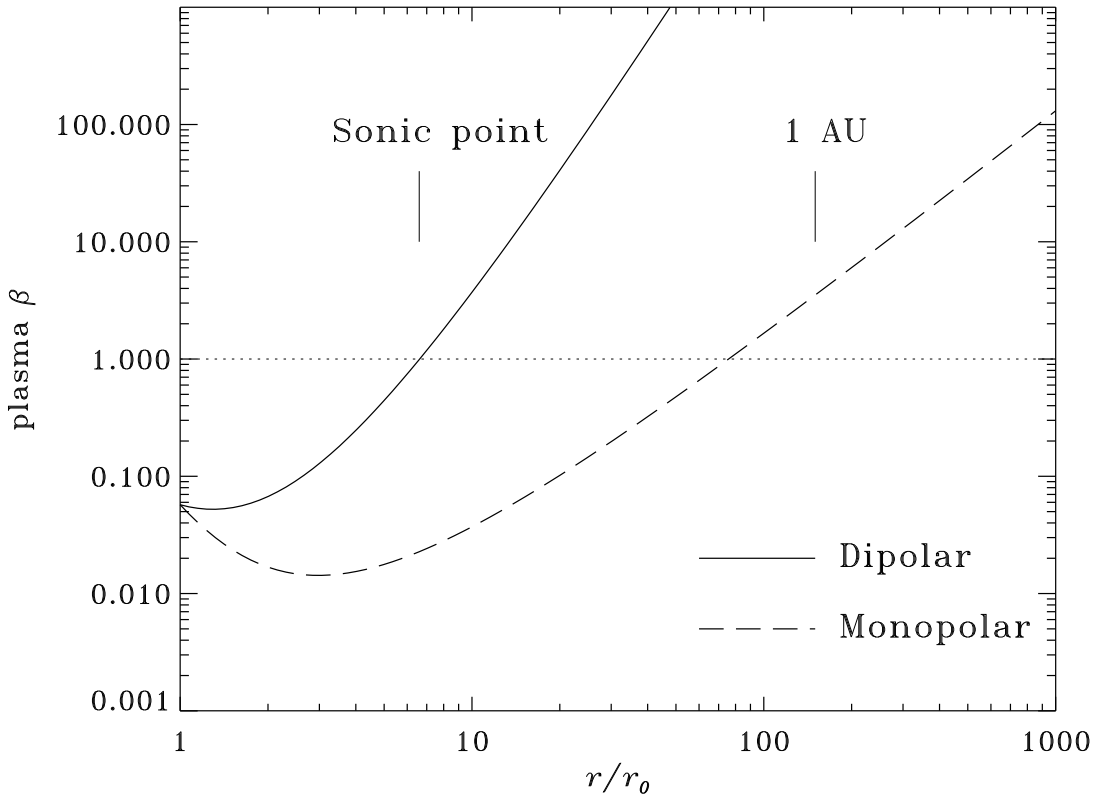

Figure 4.1: Variation of the plasma-β in the solar corona. The plasma energy is computed from the polytropic wind solution of Fig. 3.5, and the magnetic energy assuming coronal base magnetic field of 10^{-3} T, with either a monopolar ($1/r^2$) or dipolar ($1/r^3$) falloff. In either case the corona is field-dominated ($\beta \ll 1$) below the sonic point, and plasma-dominated ($\beta \gg 1$) at the Earth's orbit and beyond.

plasma-β, is defined as the ratio of gas pressure to magnetic pressure:

$$\boxed{\beta = \frac{2\mu_0 p}{\mathbf{B}^2}}\,, \tag{4.1}$$

which is basically equivalent to the ratio of thermal energy to magnetic energy. In a first approximation, when $\beta \gg 1$ the flow drags along the magnetic fieldlines, while for $\beta \ll 1$ the magnetic field either traps the plasma, or constrains it to flow along magnetic fieldlines. In which regime is the solar corona?

Computing β in the presence of a supersonic wind is complicated by the fact that the kinetic energy of the flow must also be taken into consideration, i.e., we must replace p by $p + \rho u_r^2/2$ in eq. (4.1). Figure 4.1 plots the variations with heliocentric distance of the plasma-β, for the polytropic wind solution of §3.3, and assuming either monopolar (dashed line) or dipolar (solid line) magnetic field falloffs with heliocentric distance. As argued in the preceeding chapter, the solar minimum corona lies somewhere in between these two limits.

Of course in juxtaposing in this way a radial outflow with a dipolar magnetic field, flow and field are not parallel as required by the flux-freezing constraint, but for estimating the plasma-β the procedure is justified[1]. The conclusion to be drawn from Figure 4.1 is clear: in the low corona $\beta \ll 1$, so that the magnetic field constrains plasma motions, while beyond the sonic point the high-β plasma deforms the magnetic field until $\mathbf{u}$ and $\mathbf{B}$ are parallel. For a radial

[1]Note however than in the case of the monopolar field, this is in fact a valid solution, which moreover is nowhere as silly as one might imagine (more on this shortly).

outflow, assuming a radial field is not so silly after all. At intermediate heliocentric distances we have $\beta \sim 1$, and the dynamics reflects the full complexity of the flow-field interaction... which is the central topic of the next chapter.

We now turn to two interesting aspects of solar wind dynamics that materialize in the extreme regimes $\beta \gg 1$ and $\beta \ll 1$.

4.3 The $\beta = 0$ case: magnetostatic solutions

As a prelude to our study of magnetic confinement of stellar winds, we first consider a steady-state ($\partial/\partial t = 0$) situation where the dynamics is completely controlled by the magnetic field, i.e., $\beta = 0$. If this is the case, then the problem reduces to finding a force-free field under prescribed boundary conditions at the base of the corona. We'll make the task harder by requiring that these force-free solutions look "solar-like", in the sense that they are compatible with what one would infer from coronal images such as on Fig. 3.2: an axisymmetric ($\partial/\partial\phi = 0$) dipole-like corona, with open fiedlines over the polar caps, and a streamer belt straddling the equator, with closed fieldlines low down, stretched open more or less radially above a certain height above the coronal base.

This may seem like a tall order, but it turns out that someone has already done the hard work for us, that someone being Boon-Chye Low. He constructed a family of partially-open force-free axisymmetric magnetotatic solutions, by judicious insertion of force-free current sheets into otherwise potential (i.e., current-free) solutions. Working in spherical polar coordinates (r, θ, ϕ), the starting point of the model is the specification of an axisymmetric magnetic field $\mathbf{B}(r, \theta)$ in terms of an axisymmetric **stream function** $Z(r, \theta)$ via:

$$\mathbf{B}(r,\theta) = \frac{f_B B_0}{r \sin\theta}\left[\frac{1}{r}\frac{\partial Z}{\partial \theta}\hat{\mathbf{e}}_r - \frac{\partial Z}{\partial r}\hat{\mathbf{e}}_\theta\right] \ . \tag{4.2}$$

Note that this expression will identically satisfy $\nabla \cdot \mathbf{B} = 0$, as Z can be interpreted as the z-component of a vector potential such that $\mathbf{B} = \nabla \times (Z\hat{\mathbf{e}}_\phi)$. This is really nothing fancier than the poloidal part of the toroidal/poloidal decomposition of axisymmetric magnetic fields already encountered in §1.12.3. Under this representation, Z is constant on each axisymmetric flux surface, and the value of Z can be used to label distinct such surfaces[2]. The stream function itself is constructed from two contributions:

$$Z(r,\theta;a_1,a_2) = Z_1(r,\theta;a_1) + Z_1(r,\theta;a_2) \tag{4.3}$$

where a_1 and a_2 are scale parameters, and

$$Z(r,\theta;a) = r(1-v^2)\left[(1+u^2)\mathrm{atan}\left(\frac{1}{u}\right) - u\right] - \frac{\pi a^2}{2}\frac{\sin^2\theta}{r} + 2a\eta \ , \tag{4.4}$$

with

$$u^2 = -\frac{1}{2}\left(1 - \frac{a^2}{r^2}\right) + \frac{1}{2}\left[\left(1 - \frac{a^2}{r^2}\right)^2 + \frac{4a^2}{r^2}\cos^2\theta\right]^{1/2} \ , \tag{4.5}$$

$$v^2 = -\frac{1}{2}\left(\frac{a^2}{r^2} - 1\right) + \frac{1}{2}\left[\left(\frac{a^2}{r^2} - 1\right)^2 + \frac{4a^2}{r^2}\cos^2\theta\right]^{1/2} \ , \tag{4.6}$$

$$\eta^2 = -\frac{1}{2}\left(\frac{r^2}{a^2} - 1\right) + \frac{1}{2}\left[\left(\frac{r^2}{a^2} - 1\right)^2 + \frac{4r^2}{a^2}\cos^2\theta\right]^{1/2} \ , \tag{4.7}$$

[2]This means that plotting magnetic fieldline in a meridional plane amounts to plotting contours of constant Z. Very useful property for plotting purposes!

A single parameter sequence of force-free solutions can be constructed by posing a fixed relationship between the scale parameters a_1 and a_2, e.g., $a_1 = a/2$ and $a_2 = a$. Figure 4.2 shows a sequence of four such magnetostatic solutions, for increasing values of a. These are indeed good qualitative representations of the inferred coronal magnetic at times of minimum activity (cf. Fig. 3.2).

Although this is a somewhat sadistic exercise in differential calculus, you should be able to verify that these solutions are current-free ($\nabla \times \mathbf{B} = 0$) everywhere except beyond a certain radius in the equatorial plane, with a measuring the radial equatorial extent of the closed region. However, $\mathbf{B} = 0$ there, so that the field configuration is indeed force-free ($\mathbf{J} \times \mathbf{B} = 0$). While this may all seem rather artificial, we'll see in the following chapter that fully dynamically consistent MHD axisymmetric wind solutions do look a lot like this.

How about the plasma? If we further specify that we are operating in the ideal MHD limit so that flux-freezing is enforced, then any plasma "added" a posteriori to this solution will behave very differently according to whether it is added in the magnetically closed or open region of the solutions; with plasma constrained to flow along magnetic fieldlines, in a steady-state the plasma within the closed region can only remain in hydrostatic equilibrium, while in the open regions it can in principle flow out to infinity along the magnetic fieldlines (more on this very shortly).

This duality in plasma behavior forms the basis of the **minimal energy corona conjecture** put forth some years ago by Arthur J. Hundhausen. His reasoning runs as follows: In the complete absence of plasma, the magnetic field should relax to the potential state (force-free and current-free) compatible with the lower boundary conditions on $\mathbf{B}$, as guaranteed by Aly's theorem (§1.12.4). Now, when you do problem 4.7 you will verify that the transsonic Parker-type wind solution is a minimal energy state for all possible outflow solutions, chiefly because of the large densities characterizing the fully subsonic "solar breeze" solutions (class III solutions on Fig. 3.4), and from there it is but a small step to show that the corresponding polytropic steady corona solution (§3.2) has even higher energy. So now, back to the sequence of magnetostatic solutions depicted on Fig. 4.2. As far as the plasma is concerned, the energy minimizing solution should have $a \to 0$, leading to radial fieldlines everywhere, and thus Parker-type spherically-symmetric outflow. But as far as $\mathbf{B}$ goes, the minimal energy state would here be a dipole, with $a \to \infty$ (you also get to verify this rather sweeping statement in Problem 4.7). In other words, plasma energy is a *increasing* function of the parameter a, while magnetic energy is a *decreasing* function of a. This naturally leads to the idea that a partially open configuration, with equatorial current sheet and all, represents the configuration that minimizes the *total* energy, plasma plus magnetic. This is the essence of Hundhausen's minimal energy corona conjecture.

Of course a minimal energy state is what one would expect from any closed physical system left to itself long enough to relax, but the the solar corona is anything but closed, and a number of mechanisms force it on a variety of timescales. Yet the opening and closing of magnetic arcades that accompany coronal mass ejection can indeed be interpreted as a forced destabilization opening the arcade and releasing excess plasma trapped therein, with the subsequent closing corresponding to the return to the (quasi-)steady minimal energy state. Those interested in further exploring these intringuing ideas will find pointers to the relevant literature in the bibliography at the end of this chapter.

4.4 The $\beta \ll 1$ limit: magnetic flow tubes

We already alluded to the idea that plasma could flow as a wind directed along magnetic fieldlines; the purpose of this section is to examine this channelling process in somewhat greater quantitative detail. Figure 4.3 shows fieldlines corresponding to the $a = 2.0$ magnetostatic solution discussed in §4.3, plotted in a single meridional quadrant. With plasma constrained to flow along magnetic fieldlines and base conditions (temperature, density, etc.) independent of latitude, the first thing to note is that in the region of the corona threaded by fieldlines

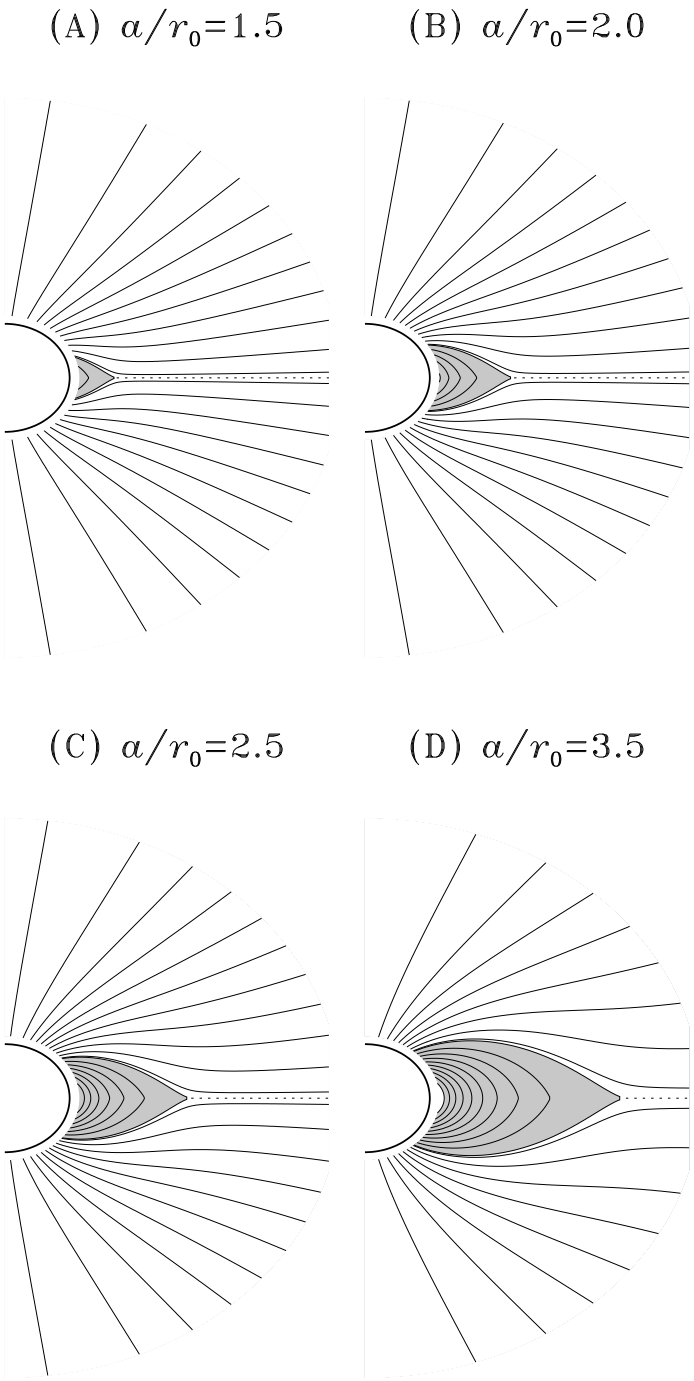

Figure 4.2: Four magnetostatic solutions defined by eqs. (4.2)—(4.7), for increasing values of the scale parameter a, as labeled. Shaded areas correspond to regions of the corona threaded by closed fieldlines, i.e., with both footpoints anchored at the coronal base. The dotted line indicates the location and extent of the equatorial current sheet.

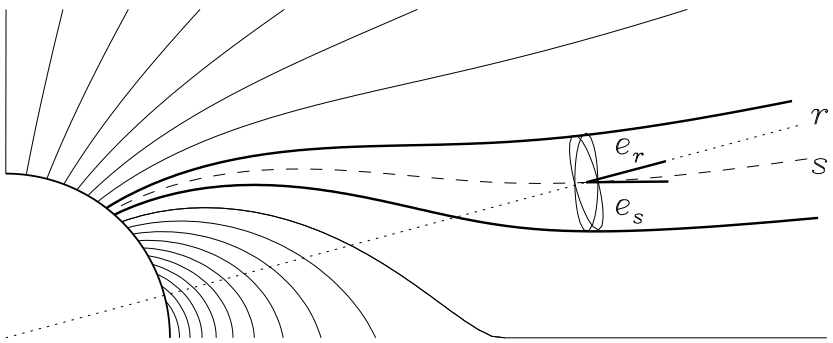

Figure 4.3: Outflow confined by a magnetic flux tube. The coordinate s (dotted line) is oriented along the central axis of the flow tube, the boundaries of which are indicated by thicker lines.

that have both footpoints anchored on the boundary, we *must* have $\mathbf{u} = 0$ to satisfy mass conservation. Indeed this has nothing to do with the field being force-free or not, it is a direct consequence of flux-freezing in a steady-state. If the magnetic field is force-free in the closed region, the force balance therein then reverts to the simple statement of hydrostatic balance encountered earlier in §3.2; if not, eq. (3.14) must be modified to include the Lorentz force, but the solution remains static.

The situation is quite different in the open region, threaded by fieldlines that extend to infinity. A wind outflow along fieldlines is now possible, but the outflow is no longer radial. Consider a narrow **flow tube** defined by two adjacent fieldlines in the open region of the magnetostatic solution (thick lines on Figure 4.3). Define a coordinate s measuring distance along the line $\mathbf{s}$ oriented along the central axis of the flow tube (dashed line on Figure 4.3). The cross-section $A(s)$ along the coordinate line is readily constructed from the known form of the magnetostatic solution.

The s-component of the equations of motion is then

$$u_s \frac{\partial u_s}{\partial s} = -\frac{1}{\rho}\frac{\partial p}{\partial s} - \frac{GM}{r^2}(\hat{\mathbf{e}}_s \cdot \hat{\mathbf{e}}_r) \tag{4.8}$$

where $\hat{\mathbf{e}}_s$ is a unit vector along the coordinate line $\mathbf{s}$. Since $\hat{\mathbf{e}}_s$ is everywhere perpendicular to the tube cross section, we have $A(r) = A(s)(\hat{\mathbf{e}}_r \cdot \hat{\mathbf{e}}_s)$ and $\partial s/\partial r \equiv \hat{\mathbf{e}}_s \cdot \hat{\mathbf{e}}_r$, eq. (4.8) becomes

$$u_s \frac{\partial u_s}{\partial r} = -\frac{1}{\rho}\frac{\partial p}{\partial r} - \frac{GM}{r^2}, \tag{4.9}$$

which means that u_s obeys an equation strictly equivalent to the r-component of the momentum equation considered in §3.3.1; a very remarkable result indeed! The only difference with the spherically symmetric solution obtained earlier is that the mass conservation statement now takes the form

$$\frac{\partial}{\partial r}\left[\rho u_r A(r)\right] = 0 \ , \tag{4.10}$$

where in general $A(r) \neq r^2$.

4.5 Generalized polytropic wind solutions

The fact that in the low-β regime magnetic fields will "rigidly" channel wind-type outflows means that the wind acceleration is akin to a nozzle flow, with magnetic flux surfaces playing the role of the nozzle's rigid boundaries, with the area expansion factor $A(s)$ acting as the

nozzle's cross-section. Now, in a polytropic flow, we already saw that the Bernoulli constant, corresponding to the total energy per unit mass, is given by:

$$E = \frac{u_r}{2} + \frac{c_s^2}{\alpha - 1} - \frac{GM}{r} \ . \tag{4.11}$$

You'll recall (hopefully) that the three terms on the RHS are, from left to right: the flow's kinetic energy, the plasma's thermal energy, and gravitational potential energy, all per unit mass. The most any nozzle can do, starting from a fluid at rest in the "combustion chamber" (here the coronal base) is to convert all of the plasma's original thermal energy into outflow kinetic energy; here this limiting velocity is given by something like:

$$u_\infty = \frac{2c_{s0}^2}{\alpha - 1} - \frac{GM}{r_0} \ , \tag{4.12}$$

where as before c_{s0} is the sound speed at r_0. But how does this work out in practice? Working once again through the mathematical steps we encountered in the case of Parker's spherically symmetric polytropic wind solution, it can be shown that for an arbitrary expansion factor $A(r)$, the r-momentum equation can be written in the following general form:

$$\frac{M^2 - 1}{2M^2} \frac{\mathrm{d}M^2}{\mathrm{d}r} = \left[1 + \left(\frac{\alpha - 1}{2}\right) M^2\right] \left[\frac{1}{A}\frac{\mathrm{d}A}{\mathrm{d}r} - \frac{1}{2}\left(\frac{\alpha + 1}{\alpha - 1}\right) \frac{GM/r^2}{(E + GM/r)}\right]$$

$$= \frac{1}{2}\left(\frac{\alpha + 1}{\alpha - 1}\right) \left[1 + \left(\frac{\alpha - 1}{2}\right)\right] \frac{1}{g}\frac{\mathrm{d}g}{\mathrm{d}r} \ , \tag{4.13}$$

where E is the Bernoulli constant of eq. (4.11), M is the Mach number

$$M(r) = \frac{u_r}{c_s} \ , \tag{4.14}$$

and the function g is given by

$$g(r) = A^{2(\alpha-1)/(\alpha+1)} \left(E + \frac{GM}{r}\right) \ . \tag{4.15}$$

The mathematics are more complex, but this is really the same general idea as with the spherically-symmetric Parker polytropic wind solution of §3.3. In particular, solutions to eq. (4.13) include sonic critical points that must be crossed by wind solution in order to avoid infinite accelerations. What is novel here is that for expansion factors with fast divergence, more than one critical points can exist in the flow. You get to explore this aspect of the problem in Problem 4.5 below.

An integral form of eq. (4.13) can also be obtained:

$$M^{4/(\alpha+1)} + \left(\frac{2}{\alpha - 1}\right) M^{-2(\alpha-1)/(\alpha+1)}$$

$$= \frac{g(r)}{g_0} \left[M_0^{4/(\alpha+1)} + \left(\frac{2}{\alpha - 1}\right)\right] M_0^{-2(\alpha-1)/(\alpha+1)} \ , \tag{4.16}$$

with $g_0 \equiv g(r_0)$ and $M_0 \equiv M(r_0)$. This is really nothing more than the Bernoulli equation (4.11) written in terms of the Mach number. This form is useful for reconstructing full wind solution, since it amounts to yet another root-finding problem for M (at fixed r).

4.6 The $\beta \gg 1$ limit: The Parker spiral

Consider now the other opposite, extreme limit of $\beta \gg 1$, in which the magnetic field is passively advected by the wind outflow. More specifically, assume a steady-state situation where

1. Flux-freezing is effectively enforced,
2. Magnetic stresses are neglected in the force balance,
3. The poloidal part of the magnetic field is purely radial in the equatorial plane, with the field strength known at the reference radius.

In view of (3), the constraint $\nabla \cdot \mathbf{B} = 0$ is readily integrated to

$$B_r(r) = B_{r0} \left(\frac{r_0}{r}\right)^2 . \tag{4.17}$$

For an average surface field $B_0 \sim 10^{-3}\,\mathrm{T}$, eq. (4.17) yields $B_r \simeq 25\,\mathrm{nT}$ at the Earth's orbit, which is not that far from the observed average magnetic field at 1AU. In view of (1), the flow streamlines coincide with magnetic fieldlines. In the absence of rotation, the Parker solution is immediately applicable. Consider now the introduction of rotation, at a rate Ω such that centrifugal effects do not affect significantly the force balance in the r-direction. In a frame co-rotating with the Sun, the wind still flows along the magnetic fieldlines. But in a stationary frame, the total velocity is now

$$\mathbf{u} = \mathbf{u}' + \Omega\, r\, \hat{\mathbf{e}}_\phi, \tag{4.18}$$

where primed quantities refer to quantities evaluated in the co-rotating frame. In general, the magnetic fieldlines are thus defined by the spiral

$$r = (u_r/\Omega_\odot)(\phi - \phi_0)\ , \tag{4.19}$$

with the r and ϕ-components of the magnetic field given by

$$B_r(r,\theta,\phi) = B_r(r_0,\theta,\phi - r\Omega_\odot/u_r) \left(\frac{r_0}{r}\right)^2 , \tag{4.20}$$

$$B_\phi(r,\theta,\phi) = B_r(r_0,\theta,\phi - r\Omega_\odot/u_r) \left(\frac{r_0\Omega_\odot}{u_r}\right) \left(\frac{r_0}{r}\right) . \tag{4.21}$$

Figure 4.4 shows, in the equatorial plane, the magnetic fieldlines defined by eqs. (4.20)–(4.21), with the dashed circle corresponding to the Earth's orbit[3]. The angle between a magnetic fieldline and the Sun-Earth radial segment is:

$$\phi_B = \arctan\left(\frac{B_\phi}{B_r}\right) = \arctan\left(\frac{r\Omega_\odot}{u_r}\right) , \tag{4.22}$$

which at 1 AU gives the rather large value $\phi_B \simeq 55^o$, which in fact compares favorably with observations. The net wind velocity at 1 AU, on the other hand, is essentially radial[4].

Now, remember the equatorial current sheet that characterized the partially open magnetostatic solutions considered in §4.3? Well this has been detected also through situ solar wind observations at 1AU. One of the most intriguing aspect of early space-borne solar wind measurements was the semi-regular polarity flips of the magnetic field carried by the wind. It was soon realized that this could be traced to the fact that the "neutral line" $B_r = 0$ at the solar surface does not coincide exactly with the equatorial circle, but is often deformed into a wavy

[3] On Fig. 4.4, is the Sun rotating clockwise or counterclockwise?

[4] Confusion on the horizon. Didn't we argue that in the flux-freezing limit, the gas could only flow parallel to the fieldlines? Shouldn't we then have $\arctan(u_\phi/u_r) \simeq 55^o$ also? How do you explain this?

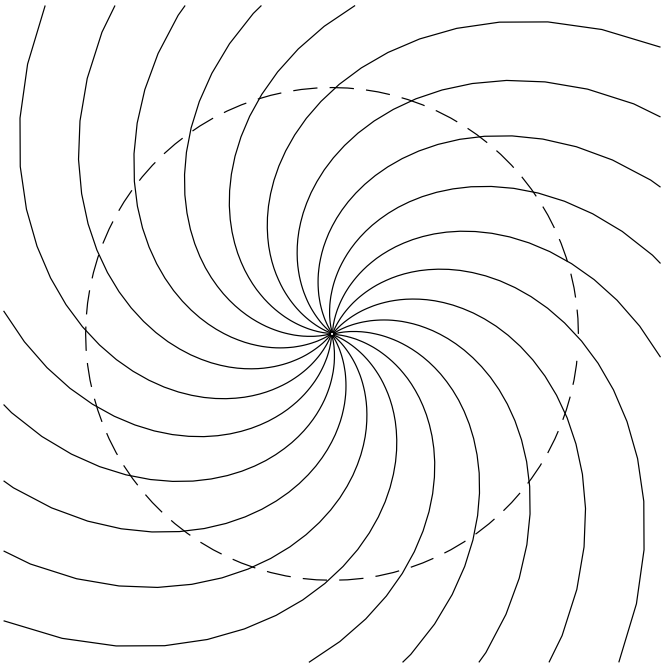

Figure 4.4: The spiral drawn by the solar magnetic field, as it is advected outward by the solar wind. Solid lines corresponds to magnetic fieldlines, and the circular dashed line to the Earth's orbit. The wind itself flows radially outward from the Sun (located at the center of the spiral, of course).

line crossing back and forth across hemispheres. This warping is maintained in the corona and solar wind, so that observations made in the ecliptic see alternately above and below the equatorial current sheet leading to apparent polarity flip as solar rotation carries this pattern along. The basic shape of this warped spiral is illustrated in cartoon form on Figure 4.5. The wavy equatorial current sheet has even been compared to the tutu of a not-so-bashful ballerina!

Problems:

1. Obtain eq. (4.1) from an appropriate dimensional analysis of eq. (1.80).
2. Work out the nozzle cross-section variation with r that would produce the same flow acceleration as in the solar wind.
3. Obtain eq. (4.12).
4. Verify that the introduction of a spherical expansion factor $A = r^2$ in eqs. (4.13)—(4.15) brings you back to eq. (3.17).
5. The aim of this (and the following) problem is to construct a polytropic wind solution for non-radial expansion factors. Consider (and, while you're at it, plot) the following function

$$f(r; R_e) = \left(\frac{1}{r^2} + \frac{R_e}{r^3} \right)^{-1}$$

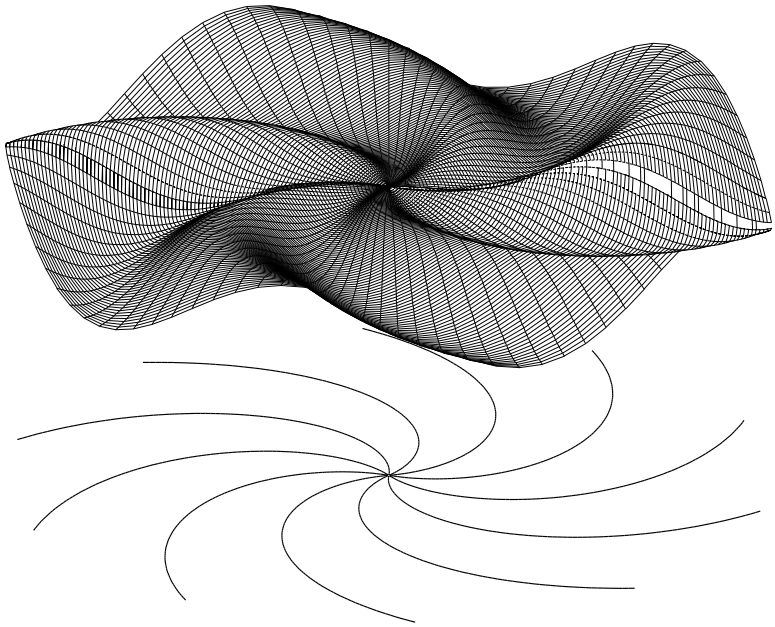

Figure 4.5: Warped spiral caused by the radial dragging of the solar magnetic field by the solar wind emanating from the rotating Sun. Any break of equatorial symmetry is imprinted on the expanding magnetic field, leading to a warping of the equatorial current sheet beyond the point where the magnetic arcades are opened up by the wind. For an observed in the equatorial plane, this leads to apparent polarity flips of the magnetic field measured in the solar wind, as one alternately "looks" above and below the current sheet.

for $R = 1$, 2 and 10. Clearly we have $\lim_{r\to 0} f(r) \propto r^3$, and $\lim_{r\to\infty} f(r) \propto r^2$, with the "turning point" occurring at $r \sim R_e$. Qualitatively, this is the kind of behavior we would get from constructing expansion factors in the polar regions of the configurations shown on Fig. 4.2. Using this expansion factor, construct a few polytropic solutions with $T_0 = 1.5 \times 10^6\,\mathrm{K}$ (e.g., consider $\alpha = 1.05$, 1.1, and 1.15) and compare the resulting flow speed and densities at 1 AU with the solar wind data for high speed streams (cf. Table 3.1). Can you generate high speed stream in this way?

6. In the lower corona, the expansion factor associated with coronal hole scales much faster than r^2 at the base of the corona. This can be modeled with the following expansion factor:

$$\frac{A(r)}{A(r_0)} = \left(\frac{r}{r_0}\right)^2 f(r)$$

with the parametric function

$$f(r) = \frac{f_m \exp((r - r_0)/\sigma) + f_1}{\exp((r - r_0)/\sigma) + 1}$$

where

$$f_1 = 1 - (f_m - 1)\exp((r_0 - r_1)\sigma)\ .$$

The quantity r_1 determines where the expansion is most pronounced, the width parameter σ controls the width of the interval in r where rapid expansion takes place, and f_m is the asymptotic expansion factor. In what follow you may set $r_1/r_0 = 1.5$ and $\sigma/r_0 = 0.1$.

Use a polytropic index $\alpha = 1.1$ and a base temperature $T_0 = 2 \times 10^6\,\mathrm{K}$, somewhat higher than the value used in the preceding chapter but in fact more appropriate for coronal holes. As usual, assume a perfect gas composed of fully ionized Hydrogen.

(a) Set the Bernoulli constant at $E = 1.8 \times 10^{-11}\,\mathrm{J\ kg^{-1}}$, and calculate the base sound speed c_{s0}, the base flow speed u_{r0} and the base Mach number M_0.

(b) Equation (4.16) being a Bernoulli-type equation, a quantity E^* defined as $E^* = \mathrm{LHS} - \mathrm{RHS}$ is directly related to the Bernoulli constant, and therefore is a constant of the flow; using your value of M_0 calculated in (a), plot, in the $[r, M]$ plane, contours of constant $E^*(r, M)$, first for a solution with purely radial expansion factor. Verify that the resulting "topology" is the same as that depicted on Fig. (3.4).

(c) Now construct outflow topologies for two rapidly diverging geometries, namely $f_m = 3$ (slow divergence) and $f_m = 12$ (fast divergence).

(d) How many critical point do you have in the "topologies" uncovered in (c)? Does the wind solution cross all of them?

If you need inspiration, consult the Kopp & Holzer paper listed in the bibliography below.

7. This one let's you explore a little bit Hundhausen's minimal energy conjecture. The first step is to verify that the Parker-like transsonic solution is the lowest-energy "coronal" solution for fixed base parameters:

(a) Start with the wind solution you computed in problem 3.6; compute the total energy associated with the wind outflow (including contributions from the plasma's internal energy, bulk kinetic energy, and gravitational potential energy);

(b) Now, keeping the Bernoulli constant E fixed at the value corresponding to the above transsonic solutions, calculate a "solar breeze" solutions (see problem 3.8), and compute its total energy content;

(c) Go back now to §3.2 and compute the total energy of the hydrostatic corona with the same polytropic index and base density as for your transsonic wind solution;

(d) Now onto the magnetic field. Using the Low (1986) force-free solutions described in this chapter, compute a one-parameter sequence of solutions (such as on Fig. 4.2) and demonstrate that the magnetic energy content increases as the magnetically closed region shrinks in size;

(e) Using all of the above results, formulate in a logically coherent manner your own version of Hundhausen's minimum energy conjecture.

If you need inspiration, consult the Charbonneau & Hundhausen paper listed in the bibliography below.

Bibliography:

The magnetostatic solutions described in §4.3 are taken from

Low, B.C. 1986, *Astrophys. J.*, **310**, 953-965,

but there is a huge literature on analytic magnetostatic coronal solutions, with or without plasma contribution to the force balance. The mathematicaly courageous wishing to look into the matter should start with

Tsinganos, K., & Low, B.C. 1989, *Astrophys. J.*, **342**, 1028.

On the minimal energy corona conjecture, see

Charbonneau, P., & Hundhausen, A.J. 1996, *Sol. Phys.*, **165**, 237-256,

and references therein. The behavior of polytropic wind solutions with rapidly diverging expansion factors is discussed in detail by

Kopp, R.A., & Holzer, T.A. 1976, *Sol. Phys.*, **49**, 43-56,

from which §4.5 is largely inspired. The spiralling extension of the Sun's magnetic field into interplanetary space by the solar wind is clearly described in

Parker, E.N. 1963, *Interplanetary Dynamical Processes* (New York: John Wiley), chap. 10.

Chapter 5

Magnetic driving of winds

We now seek to obtain wind solutions incorporating in a dynamically consistent manner the dynamical interaction between flows and magnetic fields. To do so in a mathematically tractable manner, we first compromise at the level of geometrical realism in §5.1, to obtain the justly famous Weber-Davis wind solution. Despites its geometrical restrictions, this will prove very useful in looking at the interesting problem of stellar angular momentum loss and spin-down (§5.3). We then close the chapter —and this part of the course— by looking at the possible contribution of Alfvén waves in accelerating stellar winds beyond what purely thermal driving can achieve (§5.4).

5.1 The Weber-Davis MHD wind solution

The general geometrical setup is the same as that used in obtaining non-rotating, unmagnetized polytropic wind solutions in §3.3. We consider steady ($\partial/\partial t = 0$) spherically symmetric ($\partial/\partial\theta = \partial/\partial\phi = 0$) outflow from a star rotating at angular velocity Ω and characterized by a known surface radial component of the magnetic field B_{r0}. We'll stick to the ideal MHD approximation, i.e., we set $\eta = 0$ in eq. (1.60). As before we consider the coronal base temperature $T(r_0) \equiv T_0$ as known, and do away with the energy equation by assuming a polytropic relationship between pressure and density. But here it gets a tad fishy; we will seek ouflow solutions restricted to the equatorial plane, where we impose $B_\theta = 0$. This may smell of monopolar magnetic fields, but this is really what we also did before when constructing the Parker spiral in §4.6, and the discussion of §4.3, (see in particular Fig. 4.2) indicates that a solar radius or so above the photosphere, this is a fair representation of the interplanetary magnetic field during solar minimum conditions.

A bit of reflection should convince you that we now need five input quantities to define a Weber-Davis wind model (as opposed to three for the Parker wind solution of §3.3.1):

1. the polytropic index α;
2. something measuring coronal temperature, for which we'll use the base sound speed $c_{s0} = \sqrt{\alpha p_0/\rho_0}$ at the reference radius r_0;
3. something measuring the strength of gravity; it will prove convenient to use the dimensionless ratio (γ) of the gravitational escape speed u_G ($= \sqrt{2GM/r_0}$) to the base sound speed;
4. something measuring the rotation rate, for which we can use the dimensionless parameter $\zeta = \Omega r_0/c_{s0}$;
5. something measuring the strength of the radial magnetic field component at r_0, for which we can use the dimensionless parameter $\beta = A_{r0}/c_{s0}$, where A_{r0} is the radial component of the Alfvén speed at r_0.

We group these into a solution input vector:

$$\mathbf{z} = (\alpha, c_{s0}, \gamma, \zeta, \beta) \ . \tag{5.1}$$

Let's get going. As usual, the symmetry properties imposed *a priori* on our wind solution lead to significant simplification of the governing fluid equations. Mass continuity remains what is was for the Parker wind solution of §3.3:

$$\frac{1}{r^2}\frac{\partial}{\partial r}(r^2 \rho u_r) = 0 \ , \tag{5.2}$$

while the r and ϕ-components of the momentum equation become

$$\rho\left(u_r\frac{\partial u_r}{\partial r} - \frac{u_\phi^2}{r}\right) = -\rho\frac{\partial \Phi}{\partial r} - \frac{\partial p}{\partial r} - \frac{B_\phi}{\mu_0 r}\frac{\partial}{\partial r}(rB_\phi) \ , \tag{5.3}$$

$$\rho\left(u_r\frac{\partial u_\phi}{\partial r} - \frac{u_r u_\phi}{r}\right) = \frac{B_r}{\mu_0 r}\frac{\partial}{\partial r}(rB_\phi) \ . \tag{5.4}$$

The ϕ-component of the induction equation reduces to

$$\frac{1}{r}\frac{\partial}{\partial r}(ru_r B_\phi - ru_\phi B_r) = 0 \ , \tag{5.5}$$

while the equation for the r-component is trivially satisfied (i.e., $0 = 0$!). An equation for B_r is obtained instead via the magnetic flux conservation constraint $\nabla \cdot \mathbf{B} = 0$, which here reduces to:

$$\frac{1}{r^2}\frac{\partial}{\partial r}(r^2 B_r) = 0 \ . \tag{5.6}$$

Equations (5.2), (5.6), and (5.5) integrate directly to

$$r^2 \rho u_r = C_1 \ , \tag{5.7}$$

$$r^2 B_r = C_2 \ , \tag{5.8}$$

$$r(u_r B_\phi - u_\phi B_r) = C_3 \ , \tag{5.9}$$

where C_1, C_2 and C_3 are integration constants. The first two correspond respectively to the mass and magnetic flux associated with the wind. To evaluate C_3 we transform to a reference frame co-rotating with the Sun:

$$u_\phi \to u'_\phi + \Omega r \ , \tag{5.10}$$

where the prime indicates evaluation in the co-rotating frame. Note that this (non-relativistic) transformation leaves the radial components of $\mathbf{u}$ and $\mathbf{B}$ unaffected. In that frame $\mathbf{B}$ is stationary, and since we are working under the flux-freezing approximation $\mathbf{u}$ and $\mathbf{B}$ must be parallel:

$$\frac{u'_r}{u'_\phi} = \frac{B'_r}{B'_\phi} \ . \tag{5.11}$$

Since $B_r = B'_r$, eq. (5.9) yields

$$C_3 = -\Omega r^2 B_r \ , \tag{5.12}$$

so that

$$B_\phi = \frac{B_r}{u_r}(u_\phi - \Omega r) \ . \tag{5.13}$$

Now, eq. (5.4) can obviously be rewritten as

$$\frac{\partial}{\partial r}(ru_\phi) = \frac{B_r}{\mu_0 \rho u_r}\frac{\partial}{\partial r}(rB_\phi) \ ; \tag{5.14}$$

but in view of eqs. (5.7) and (5.8), we have $B_r/\mu_0\rho u_r = C_2/\mu_0 C_1$, i.e., a constant! Which means that eq. (5.14) integrates immediately to

$$ru_\phi - \frac{rB_\phi B_r}{\mu_0 \rho u_r} = L \ , \tag{5.15}$$

where L is yet another integration constant. It has a well-defined physical meaning, as it corresponds to the total angular momentum carried away by the wind, which is made up of two contributions: the specific angular momentum of the expanding fluid (first term on LHS), and the torque density associated with magnetic tension (remember that the magnetic field is being dragged away by the wind outflow!)

The results of all this algebraic juggling, without giving us a full wind solution, still allow us to draw some interesting conclusions regarding the behavior of the outflow. First we rewrite eqs. (5.13) and eqs. (5.15) in terms of the components of the Alfvén velocity[1] (§1.8):

$$A_r = \frac{B_r}{\sqrt{\mu_0 \rho}} \ , \qquad A_\phi = \frac{B_\phi}{\sqrt{\mu_0 \rho}} \ , \tag{5.16}$$

leading to

$$A_\phi = \frac{A_r}{u_r}(u_\phi - \Omega r) \ , \tag{5.17}$$

$$u_\phi = \frac{L}{r} + \frac{A_r A_\phi}{u_r} \ . \tag{5.18}$$

Substituting now for A_ϕ in eq. (5.18) and making good use of eqs. (5.16) and eqs. (5.17) yield, after some straightforward algebra:

$$u_\phi = \Omega r \frac{(u_r^2 L/\Omega r^2) - A_r^2}{u_r^2 - A_r^2} \ . \tag{5.19}$$

Look at the denominator of this expression; clearly, if the radial flow velocity ever becomes equal to the radial Alfvén speed, we are in trouble... unless the numerator also happens to vanish. We can save the day in this way provided we set

$$\boxed{L = \Omega r_A^2} \ , \tag{5.20}$$

where r_A is the **Alfvén radius**, defining the spherical shell where $u_r = A_r$. Now, remember that L is the total angular momentum carried away by the wind, *including* the torque density provided by magnetic tension. Equation (5.20) states that this is equal to the angular momentum that would be carried away by an unmagnetized wind flowing strictly radially, and co-rotating with the solar/stellar surface out to radius r_A. We are going to get a lot of mileage from this remarkable result later on. But let's first try to get a full wind solution. Go back to the r-component of the equation of motion (eq. (5.3)); use eq. (5.13) to eliminate B_ϕ in the

[1] Please do not confuse the "A" here with components of the magnetic vector potential...

last term on the RHS; then use eq. (5.13) to eliminate the B_ϕ derivative multiplying u_ϕ (but leave the one multiplying Ω alone!). Somewhat tedious algebra eventually leads to

$$\frac{\partial}{\partial r}\left[\frac{1}{2}(u_r^2+u_\phi^2)-\frac{GM}{r^2}+\frac{c_{s0}^2}{\alpha-1}\left(\frac{\rho}{\rho_0}\right)^{\alpha-1}-\frac{r\Omega A_r A_\phi}{u_r}\right]=0\ , \tag{5.21}$$

where the magnetic field components are again expressed in terms of their corresponding Alfvén speed components, and the polytropic approximation was used to deal with the pressure gradient term. This indicates that the quantity within the square brackets must be a constant[2]. This is again a Bernoulli-type statement for the flow, expressing conservation of energy, and as before we will denote the quantity in square brackets by E.

Obtaining a full solution (i.e., u_r, $u_\phi(r)$, etc.) is now a much more complicated procedure. The starting point is the manipulation of eq. (5.3) into the form:

$$\frac{\partial u_r}{\partial r}=\left(\frac{u_r}{r}\right)\frac{(u_r^2-A_r^2)(2c_s^2+u_\phi^2-GM/r)+2u_r u_\phi A_r A_\phi}{(u_r^2-A_r^2)(u_r-c_s^2)-u_r^2 A_\phi^2}\ , \tag{5.22}$$

which involves some straightforward but tedious algebraic juggling. Now, that denominator looks like trouble once again. It actually vanishes whenever the radial flow speed u_r becomes equal to the phase speed of either the slow or fast magnetosonic wave modes[3], which in general occurs at distinct radial distances denoted r_s and r_f in what follows. Denote now by N and D the numerator and denominator on the RHS of eq. (5.22); to avoid divergence at r_s or r_f we require that

$$N(r_f,u_f)=0\ , \tag{5.23}$$
$$D(r_f,u_f)=0\ , \tag{5.24}$$
$$N(r_s,u_s)=0\ , \tag{5.25}$$
$$D(r_s,u_s)=0\ , \tag{5.26}$$

complemented by the requirement that solutions running through the two critical points should also be characterized by the same value of the Bernoulli constant[4]:

$$E(r_f,u_f)=E(r_0,u_{r0})\ , \tag{5.27}$$
$$E(r_s,u_s)=E(r_0,u_{r0})\ . \tag{5.28}$$

These expressions represent a set of six coupled nonlinear algebraic equations that must be solved simultaneously for a "solution vector"

$$\mathbf{w}=(u_{r0},u_{\phi 0},r_s,u_s,r_f,u_f)\ . \tag{5.29}$$

Well, we can find reassurance in the fact that we have as many equations as we have unknowns, but the fact remains that solving this nonlinear algebraic system is A BEAR of a root finding problem. It can be turned into a (somewhat easier) optimization problem, by seeking solutions that minimize the sum of the squared N's, D's and E's, but even then you better have a pretty good initial guess for the solution vector to start a conjugate gradient or whatever, because the

[2]If eq. (5.21) doesn't look at least a bit familiar, go back and read chapter 3, before proceeding, because you're already in trouble enough.

[3]Remember that these correspond to sound-like longitudinal waves for which the sum of gas and magnetic pressures act as a restoring force; if both are in (out of) phase, the magnetosonic wave is fast (slow). If you don't remember, `goto` §1.8, do not pass GO, do not collect $200

[4]Hold on now, didn't we say a little while back that the wind also had to go through the Alfvén point, to avoid a blowup of the azimuthal velocity, as per eq. (5.19)? Well it turns out that in the Weber-Davis-type wind models, any solution going through the slow and fast magnetosonic points (r_s,u_s), (r_f,u_f) *automatically* goes through the Alfvén point (r_A,u_{rA}). Skeptics should either get a life, or consult Goldreich & Julian 1970, ApJ, 160, 971.

6-dimensional search space is very multimodal. But it can be done; and if you do it for the "solar" input vector

$$\mathbf{z}_\odot = (1.1, 165., 0.01415, 3.495, 3.688) \ , \tag{5.30}$$

you find a "solar" solution vector

$$\mathbf{w}_\odot = (0.0123, 0.0140, 6.60, 0.676, 29.5, 1.378) \ , \tag{5.31}$$

where the flow speeds are expressed in fractions of the base sound speed c_{s0}, and the critical point radii in units of the reference radius r_0. Reconstructing a full solution is a lengthy but straightforward process which involves the following sequential steps:

1. Construct $A_r(r, u_r)$; this is a function of B_r and ρ, B_r is only a function of r as per eq. (5.8), and ρ of u_r and r via eq. (5.2).

2. With A_r known, construct $u_\phi(r, u_r)$ via eq. (5.19), evaluating the constant L at r_0:

$$L = r_0 u_{\phi 0} \left[1 - \left(\frac{A_{r0}}{u_{r0}} \right)^2 \right] + \Omega r_0^2 \left(\frac{A_{r0}}{u_{r0}} \right)^2 \ . \tag{5.32}$$

3. B_ϕ (and thus A_ϕ) can now be constructed using eq. (5.17).

This gives us all the needed pieces to express the Bernoulli constant E (cf. eq. (5.21)) in terms of r and u_r only. Setting then

$$E(r_0, u_{r0}) = E(r, u_r) \tag{5.33}$$

brings us back to a one-dimensional root finding problem, which we've handled before. Once we have u_r, $\rho(r)$ follows immediately from eq. (5.2). Knowing B_r/B_{r0} from eq. (5.8), u_ϕ is evaluated using eq. (5.19), and finally A_ϕ via eq. (5.17), AND THAT'S FINALLY IT!

The resulting solar solution is plotted on Figure 5.1, with some strategic numbers listed in Table 5.3. The purely hydrodynamical components of the solution having a counterpart in the unmagnetized, non-rotating solar wind solution obtained in §3.3, i.e. u_r, ρ, and $T(r)$, look an awful lot similar to Parker's solution. The notable difference is that the flow is no longer purely radial but now has a non-vanishing ϕ-component (as measured by the flow's pitch angle $\phi_v \equiv \mathrm{atan}(u_\phi/u_r)$), quite important near r_0 but falling off rapidly with increasing radial distance. Yet the value computed at Earth's orbit is in agreement with *in situ* mesurements. That's certainly something worth celebrating.

Table 5.3
Weber-Davis solar wind solution

r	u_r [km s^{-1}]	N [10^6 m^{-3}]	T [K]	ϕ_v [deg]	ϕ_B [deg]
r_0	2.0	10^8	1.5×10^6	48.7	-0.59
r_s	115	37400	6.8×10^5	4.01	-3.95
r_f	231	891	4.7×10^5	2.00	-15.7
$r_\oplus$	319	17	3.1×10^5	0.53	-54.5
$10\, r_\oplus$	380	0.14	1.9×10^5	0.06	-81.0

Nonetheless, after all this work, it is almost disappointing how little our solar WD wind solution differs from its non-rotating, unmagnetized counterpart of §3.3. This is due, to a large extent, to the relatively low rotation rate of the Sun, and to its relatively low magnetic field strength (refering here to the global-scale, diffuse coronal magnetic field, not that immediately overlying sunspots and active regions). But in other parameter regimes the differences become striking indeed. Consider for example the WD solution depicted on Figure 5.2; this corresponds

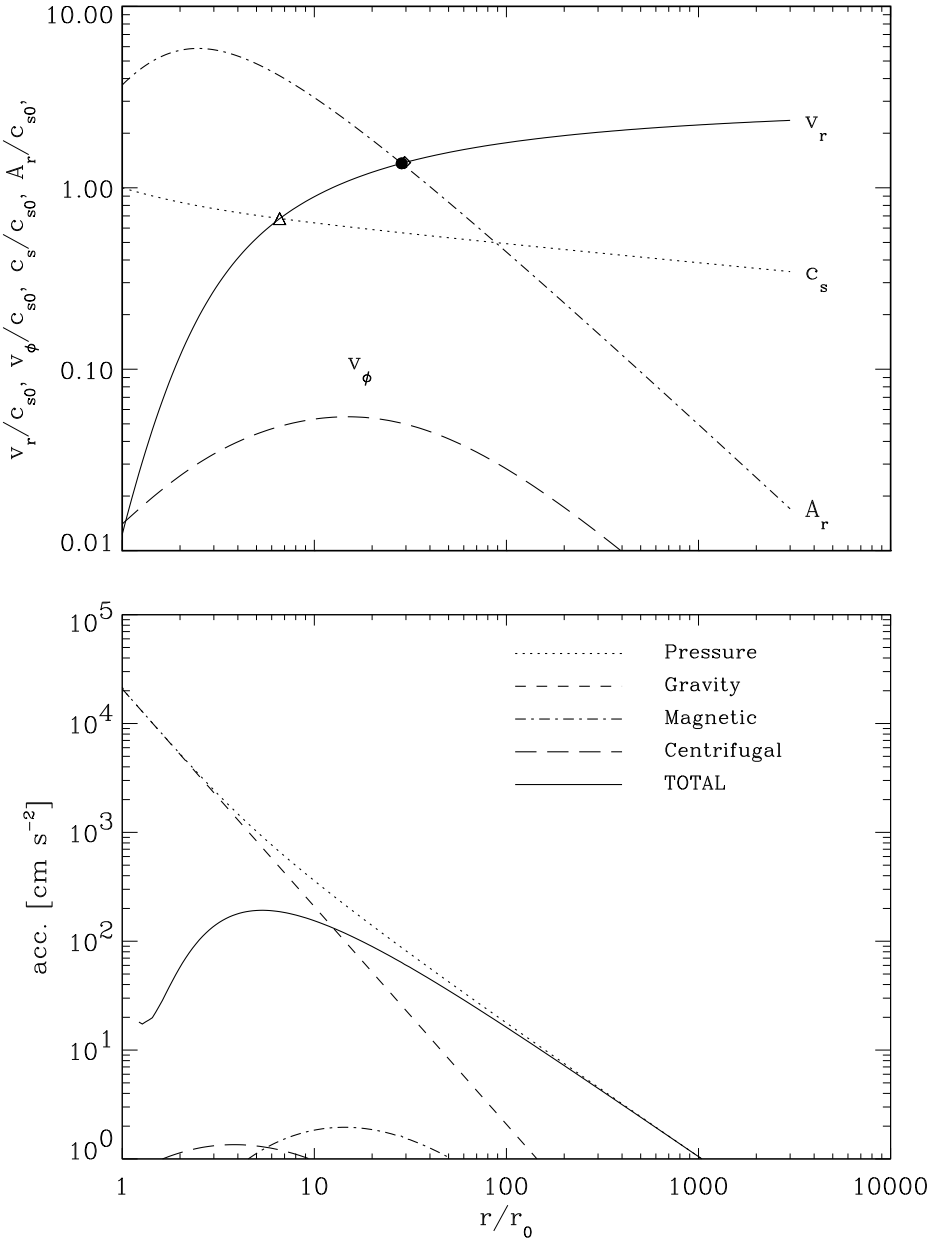

Figure 5.1: The full solution for the WD wind model with solar-like input parameters. The top panels shows the wind properties, with the slow magnetosonic point indicated by a triangle, the Alfvén point by a solid dot, and the fast magnetosonic point by a diamond (here almost coincident with the Alfvénic critical point). The bottom panel shows details of the force balance in the wind.

to a Sun-like star, still with a $T_0 = 1.5 \times 10^6\, K$ corona and polytropic index $\alpha = 1.1$ as before, but now rotating at 25 times the solar angular velocity, and with a surface field strenth also increased by a factor 25. The flow speed at large distances now exceeds the local sound speed by nearly two orders of magnitude, meaning a Mach 100 flow! The azimuthal velocity u_ϕ now exceeds the radial flow speed inside the slow magnetosonic point, and remains comparable to it out to the Alfvén point. These dramatic difference can be traced to the centrifugal and magnetic contributions to the force balance (bottom panel). While the flow remains mostly thermally-driven near the base of the corona, within a few r_0 the centrifugal and magnetic accelerations become comparable to the pressure gradient term, and completely dominate the dynamics thereafter. You may verify that the asymptotic flow speed is now given by

$$\lim_{r\to\infty} \equiv u_{r\infty} \simeq \left(\frac{\Omega^2 r_0^4 B_{r0}^2}{\dot{M}} \right)^{1/3} , \tag{5.34}$$

with $\dot{M} = 4\pi\rho_0 r_0^2 u_{r0}$ as in §3.3.

Figure 5.3 shows the variations with distance of the two contributions to angular momentum loss in the WD wind solutions of Figs. 5.1 and 5.2. Note how the rapidly rotating, strongly magnetized wind carries away a lot more angular momentum than in the solar solution. In view of eq. (5.15) one may have expected a factor of 25 coming from the Ω dependency, but the Alfvén point also moves outwards by a factor of nearly four (cf. Figs. 5.1 and 5.2, solid dots on top panels). In fact, it is (relatively) easy to show that in the limit of weak centrifugal and magnetic driving,

$$r_A \simeq \frac{r_0^2 B_{r0}}{\sqrt{\dot{M} u_{r\infty}}} , \tag{5.35}$$

as opposed to

$$r_A \simeq \sqrt{\frac{3}{2}} \frac{u_{r\infty}}{\Omega} \tag{5.36}$$

for the rapidly rotating, strongly magnetized wind solution of Fig. 5.2.

5.2 Numerical models of rotating MHD winds

The Weber-Davis solution of §5.1 is applicable only in the equatorial plane; but could we not "project" it on conical surface of decreasing opening angle to reconstruct an axisymmetric solution in a full meridional $[r, \theta]$ plane? As you get to verify in Problem 5.3 below, this leads to an unbalanced latitudinal gradient of magnetic pressure. Moreover, the monopolar magnetic configuration of the Weber-Davis solution should cerainly be improved upon.

In obtaining fully two-dimensional Weber-Davis-like wind solutions there is no recourse but a approach that is numerical from the onset. We will now look in to such numerical solutions, computed a few years ago by R. Keppens and H. Goedbloed (see bibliography). These solutions are particularly interesting because they are Weber-Davis-like in a number of ways: steady ($\partial/\partial t = 0$), axisymmetric ($\partial/\partial\phi$) and polytropic ($\alpha = 1.13$), and computed in the ideal MHD limit. The magnetic configuration they simulate is qualitatively similar to the magnetostatic solution depicted on Fig. 4.2, in that in contains a closed-fieldline region symetrically straddling the equator, and open fieldline regions over the poles. In addition to the magnetic field strength and rotation parameter, a third parameter is now introduced to set the latitudinal extent of the closed field region (often called "dead zone" because **u** must vanish therein, due to the flux-freeezing constraint imposed by ideal MHD). The solutions are obtained as a time-dependent relaxation problem, starting with a purely hydrodynamical rotating wind solution, and a magnetic field patched up as a combination of a dipole for the closed region, and split monopole for the open regions. The solution is then integrated forward in time until a steady-state is attained.

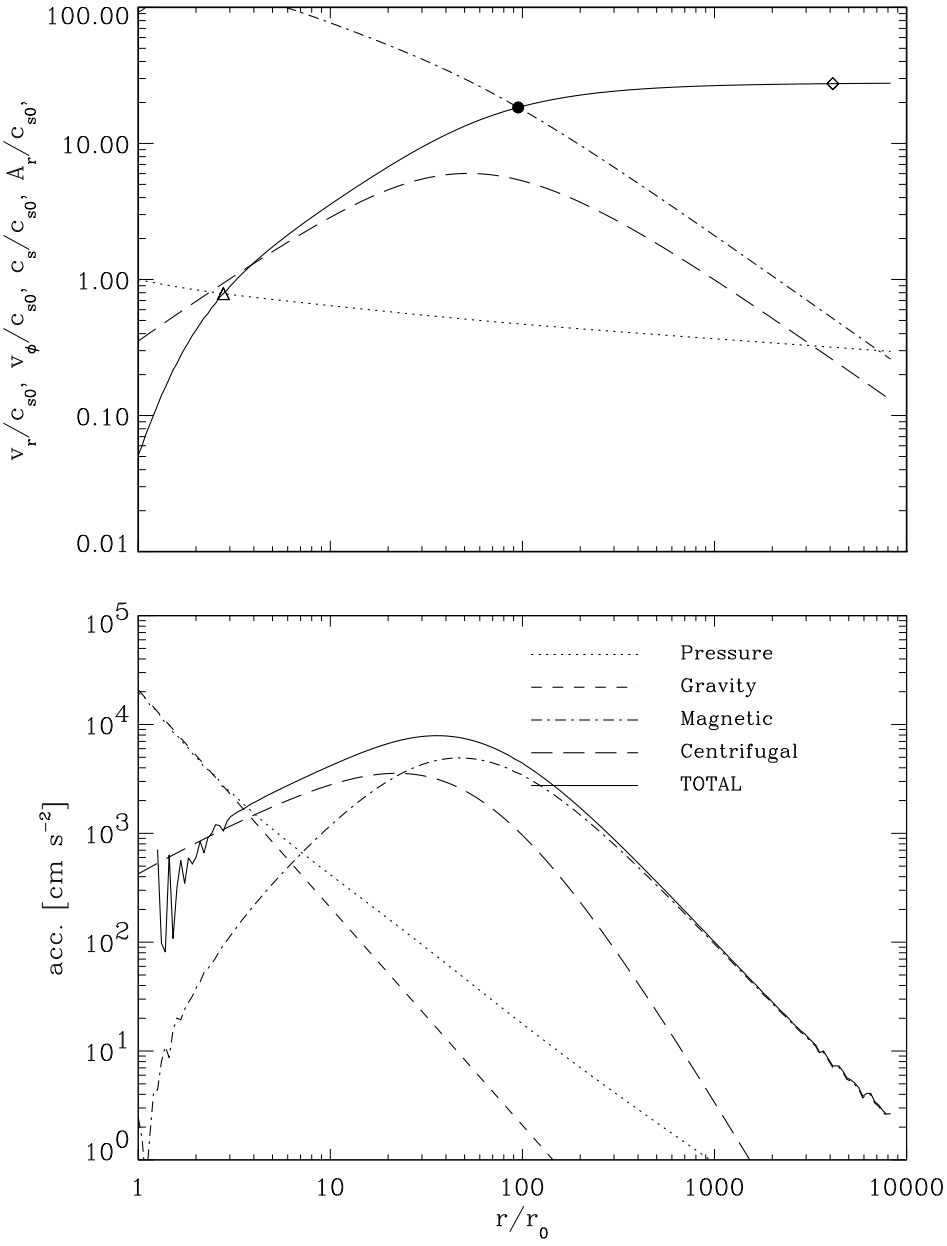

Figure 5.2: Similar to Fig. 5.1, but now for a solar-like star that is rapidly rotating ($\Omega = 25\Omega_\odot$) and strongly magnetized ($B_{r0} = 25B_{r0,\odot}$), representative of a young solar-type star. Note how the magnetic tension force is now the primary contributor to the wind's acceleration at large distances.

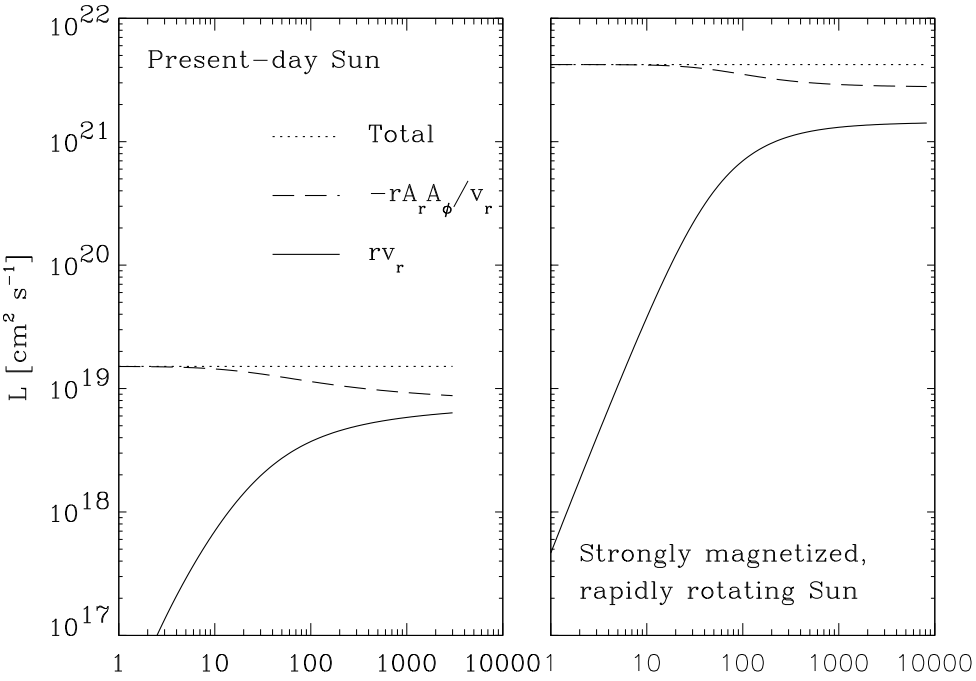

Figure 5.3: Contributions to the total angular momentum carried away by the wind for the two WD solutions depicted on Figs. 5.1 (left) and 5.2 (right). The solid line is the angular momentum per unit mass, and the dashed line the torque density produced by magnetic tension in the deformed magnetic field. The sum of these two contributions (dotted line), the total specific angular momentum, is a constant of motion, as per eq. (5.15).

The top panel on Figure 5.4 shows a solar-like solution, with a 2G polar field strength and a closed region extending $\pm 30^\circ$ on either side of the equator. Note first how the wind outflow is directed along the magnetic fieldlines, as it must in a steady state as per the flux-freezing constraint characterizing ideal MHD. At mid-latitude, the solution shows many similarities to the Weber-Davis solution of Fig. 5.1. The slow magnetosonic surface is well within the Alfvén critical surface, and the latter very nearly coincide with the fast magnetosonic surface (these were all critical points in the 1D WD solution of §5.1, cf. the triangle, diamond and solid dot on Fig. 5.1). At low latitudes, the effect of the closed field region alters the flow quite significantly, although beyond $10\,R_\odot$ or so the wind speed is comparable to that at high latitudes. The wind density, however, is larger by about a factor of three. Close examination of the Figure will reveal that the outflow speed has a poleward-directed latitudinal component, which turns out to be very well fitted by a $\sin(2\theta)$ dependency at heights much larger than the radial extent of the closed field region.

As can be seen on the bottom panel of Figure 5.4, doubling the field strength and latitudinal extent of the magnetically closed region leaves these basic solution characteristics unaltered. Not surprisingly, away from the closed region the solution is characterized by a greater degree of spherical symmetry, which is what is to be expected in a split-monopole configuration where the field is better able to channel the flow without being distorted. Indeed, the shape of poloidal fieldlines (solid lines) show a striking resemblance to those characterizing the magnetostatic solutions considered in §4.3 (cf. Fig. 4.2).

Figure 5.5 depicts yet another wind solution, this time for a sun rotating at 20 times its present rate, but maintaining the same surface magnetic field configuration and strength as on Fig. 5.4A. The impact of this high rotation rate on the wind is substantial in many ways. As on the Weber-Davis solution of Fig. 5.2, the fast magnetosonic surface is now well-

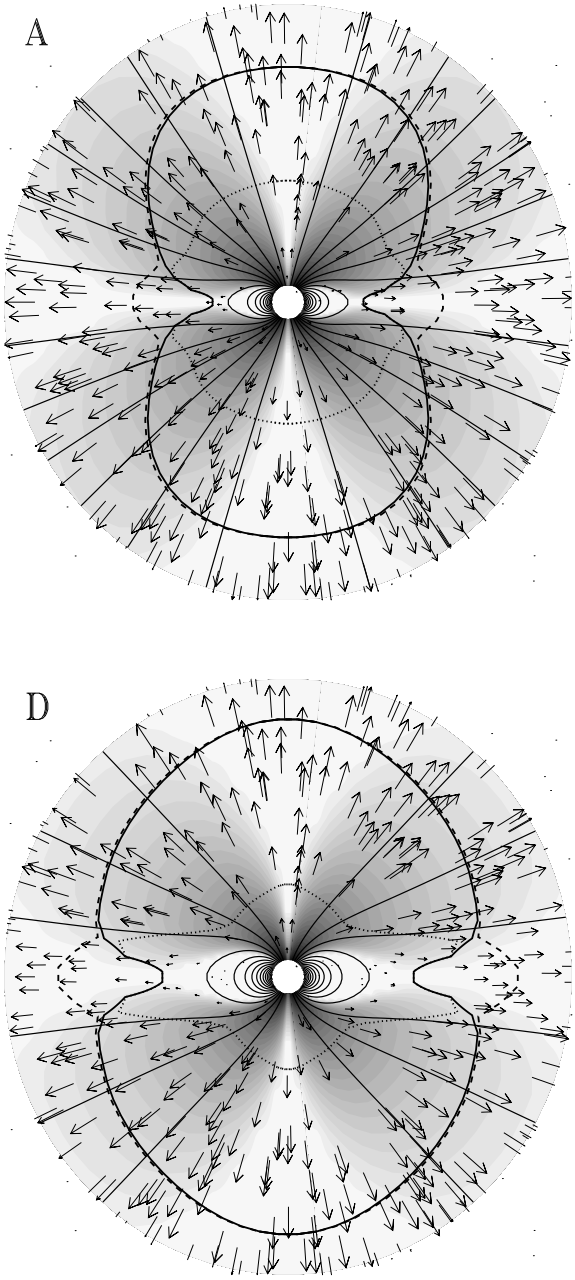

Figure 5.4: Axisymmetric 2D MHD model of the solar wind. The flow field is indicated as vector, the poloidal magnetic fieldlines by solid lines, and the gray scale encodes the strength of the toroidal magnetic component. The dotted, dashed and thick solid lines are respectively the slow and fast magnetosonic surfaces, and the Alfvén surface. The top solution is for present-day solar parameters, while the bottom solution pertains to a strongly magnetized sun (see text). Graphics courtesy of Rony Keppens (U. Leuven).

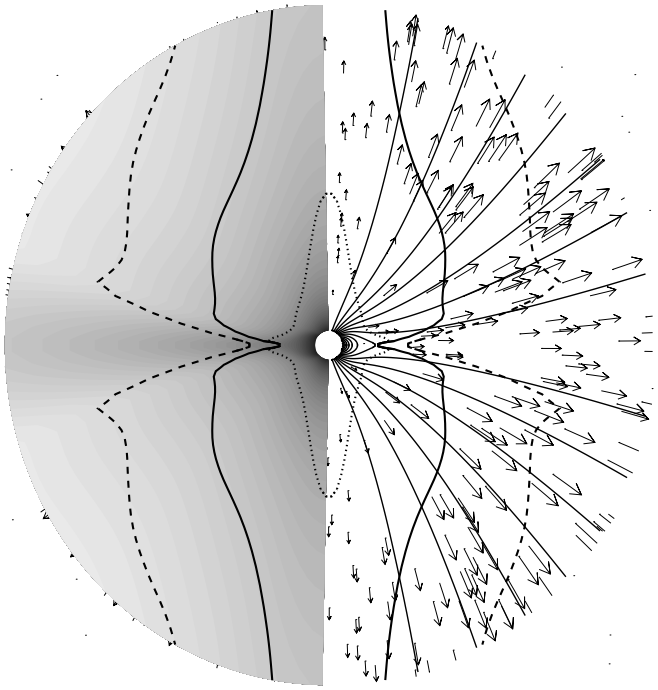

Figure 5.5: Similar to Fig. 5.4A, but for a sun rotating at 20 times its present rotation rate. The grayscale on the left now encodes the density, rather then the toroidal field strength. Note the poleward collimation of the wind into a polar jet, and the density excess in the equatorial plane. Graphics courtesy of Rony Keppens (U. Leuven).

separated from the Alfvén surface. Rotation leading to tighter winding of the magnetic field, the latitudinal magnetic pressure gradient associated with the strong toroidal field component leads to a collimation of the wind towards the poles. In addition, efficient magnetocentrifugal driving at low latitudes leads to enhanced densities in and near the equatorial plane.

5.3 Stellar spin-down

Even though it is primarily thermally-driven, the solar-like WD solution of Fig. 5.1 is losing far more angular momentum than in the absence of magnetic fields, as per eq. (5.20). This, it turns out, goes a long way in explaining the very peculiar distribution of observed stellar rotational velocities on the main-sequence.

5.3.1 Stellar rotation: the observational picture

The rotation of a star other than the Sun as first measured serendipitously at the beginning of this century by F. Schlesinger, in the brighter component of the eclipsing binary δLibrae at occultation. Subsequent determinations of rotation rates for single stars relied on the Doppler broadening of spectral lines, as originally suggested by W.W. Abney in 1877, but first succesfully executed much later, in 1929, by C.T. Elvey. For a single star, this projected rotational velocity ($v \sin i$) yields only a lower limit on the true equatorial rotation rate, as the angle i between the line of sight and the star's rotation axis is generally unknown.

As increasingly sensitive spectroscopic determinations of $v \sin i$ for a growing sample of single stars accumulated, the existence of systematic differences between the average rotation rates for late-type versus early-type stars was soon noted. Figure 5.6 below is a reproduction of a diagram put together by R. Kraft in 1967, showing the distribution in a HR diagram of $v \sin i$'s measured in a sample of field stars. As one runs down the main sequence, there occurs a sharp drop in $v \sin i$ starting around spectral type F5. Slow rotation is the rule on the cool side of this so-called rotational dividing line, while on the hot side rapid rotation is common. Kraft went on to show that under the assumption of solid-body rotation, in the interval $1.5 \lesssim M/M_\odot \lesssim 20$ observed rotation rates are consistent with a power-law dependence betwen stellar angular momentum (J) and mass (M) of the form

$$J \propto M^{1.57} \ . \tag{5.37}$$

It was already understood then that the decrease in the moment of inertia of stars associated with their contraction towards the main-sequence could easily account for ZAMS equatorial rotational velocities of a few hundreds of kilometers per second, so that the anomaly in Kraft's diagram was in fact with the slowly-rotating low-mass stars. Rather than some strongly mass-dependent process (such as proto-early-type-stars diverting a substantial fraction of their spin angular momentum into planetary orbital angular momentum, for example), the favored interpretation back then was already that late-type stars somehow lose angular momentum on the main-sequence, i.e., they undergo spin-down.

Spectacular evidence for such main-sequence spin-down was provided in a short, now classical 1972 paper by Andy Skumanich[5]. Figure 5.7, reproduced from this paper, illustrate the gradual decrease of average rotation rates for late-type stars in a few (young) open clusters of known ages. Skumanich also noted a similar decrease of emission in the core of the Ca H and K lines, which as you CERTAINLY remember from chapter 2 is a good proxy of magnetic activity. This established a first empirical, quantitative link between rotation and magnetic activity, to which we shall return in due time.

Later observations focusing on young open clusters such as αPersei and the Pleiades have revealed that main-sequence spin-down for late-type stars is very swift, with the bulk of it completed in the first few 100 Myr after arrival on the ZAMS.

5.3.2 The Skumanich square-root law

In case you haven't seen it coming yet, our WD wind models provide us with some of the key physical pieces required to understand main-sequence spin-down. Towards this goal, the most important result obtained in §5.1 is eq. (5.20), stating that the total angular momentum per unit mass (L) carried away by the wind is equal to that which would be carried away by an unmagnetized wind remaining in a state of strict co-rotation out to the Alfvén radius r_A:

$$L = \Omega r_A^2 \ . \tag{5.38}$$

To obtain the net angular momentum loss, we just need to multiply L by the wind's mass flux. However, eq. (5.38) holds only in the equatorial plane, where the WD solution is computed. We need to construct an equivalent expression for the whole sphere, which is *not* simply $4\pi\Omega r_A^2$. Remember that what matters for angular momentum extraction is the component of the flow moving away perpendicularly to the rotation axis. The WD model can be "stretched" to the whole sphere by assuming that a whole spherical shell is co-rotating out to r_A; this means replacing eq. (5.38) by:

$$L_{\rm sph} = \frac{2}{3}\Omega r_A^2 \ , \tag{5.39}$$

[5]Still today affectionately know to his HAO colleagues as Doctor Slamdunk

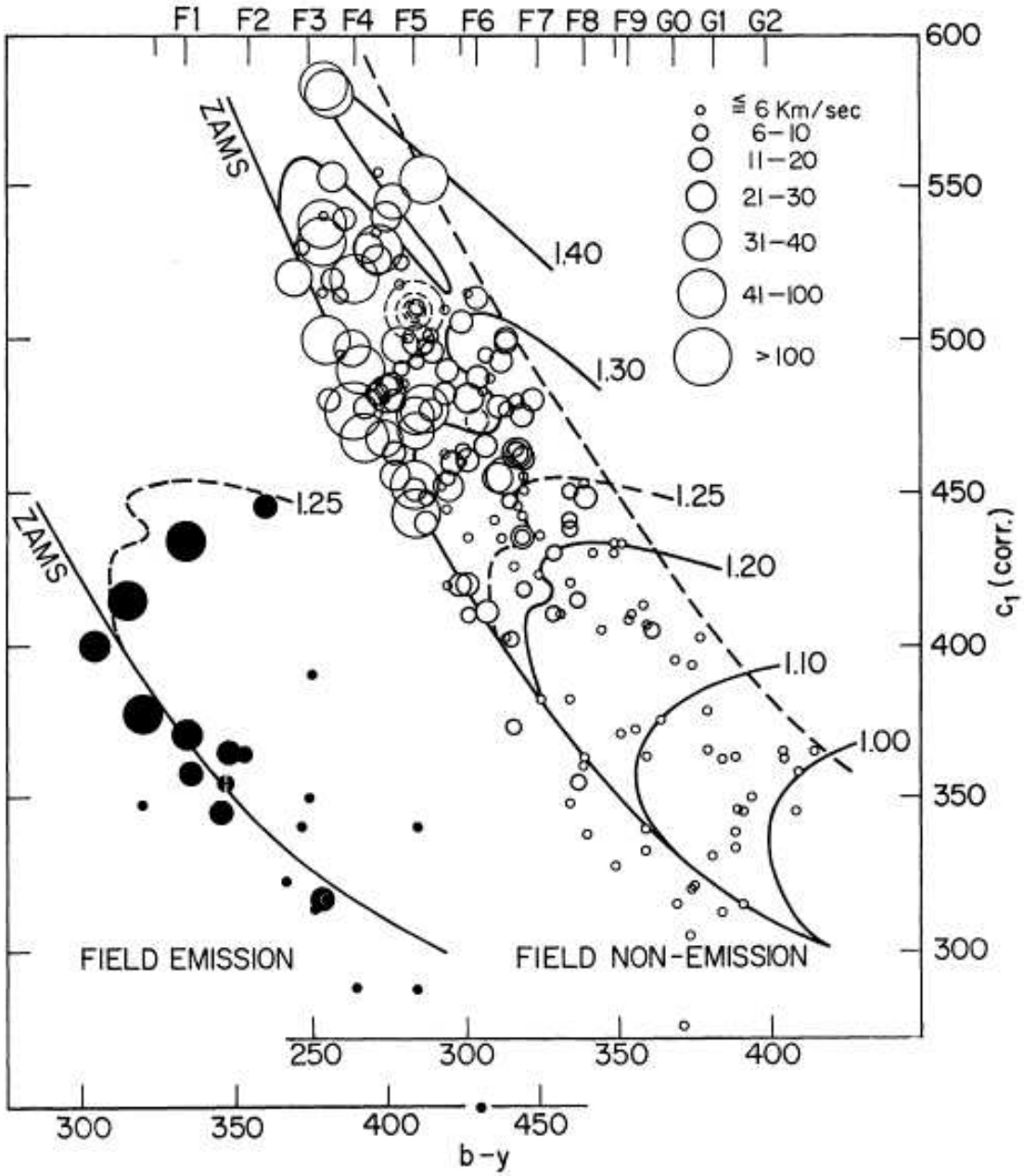

Figure 5.6: Distribution of projected rotational velocities ($v \sin i$) for main-sequence stars, plotted in an observational HR diagram. Luminosity increases vertically upwards, and effective temperature horizontally leftward. Astronomical spectral types are listed along the upper axis. Solid lines are stellar evolutionay tracks, labeled according to mass in solar units. These tracks, particularly for $M/M_\odot \gtrsim 1.2$, are now somewhat obsolete. Diagram reproduced from Kraft, R. 1967, ApJ, 150, 551 (Figure 1, p. 558).

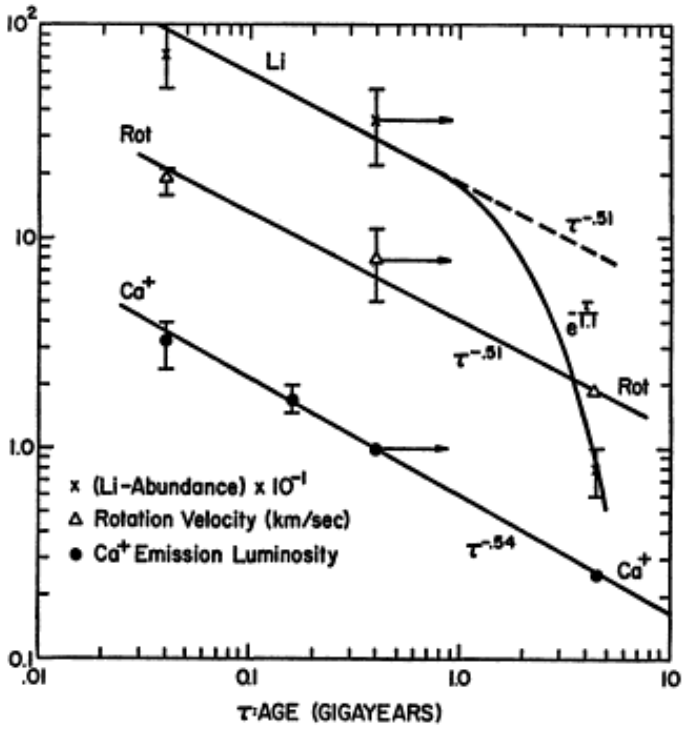

Figure 5.7: Main-sequence temporal evolution of rotation rates, Calcium emission and Lithium abundance in solar-type stars. Diagram reproduced from Skumanich, A. 1972, ApJ, 171, 565 (Figure 1, p. 566).

where the factor 2/3 simply arises from the moment of inertia. The angular momentum loss rate then follows directly:

$$\frac{\mathrm{d}J}{\mathrm{d}t} = \dot{M} \times L_{\rm sph} = -4\pi\rho_A r_A^2 u_{rA} \left(\frac{2}{3}\Omega r_A^2\right) \ . \tag{5.40}$$

Now, at the Alfvén radius we have $u_{rA} = A_{rA}$, with $B_{rA}^2 = 4\pi\rho_A A_{rA}^2$. Moreover, conservation of magnetic flux implies $r_0^2 B_{r0} = r_A^2 B_{rA}$. Putting all this into eq. (5.40) leads to

$$\frac{\mathrm{d}J}{\mathrm{d}t} = \dot{M} \times L_{\rm sph} = -\frac{2}{3} B_{r0}^2 r_0^4 \Omega A_{rA}^{-1} \ . \tag{5.41}$$

Now, for rotating magnetized winds that are mostly thermally driven (as on Fig. 5.1), we have $A_{rA} \sim c_s$ to within a factor of two or so. If the coronal temperature is held fixed, this means that the angular momentum loss rate is only a function of the rotation rate and surface magnetic field strength. Both are known for the Sun, but how about the "young Sun" of 4.5 Gyr ago? If stars of one solar mass in αPersei or the Pleiades are representative of the ZAMS Sun, then its rotation could have been anywhere between 5 and 100 times its present value. How about its surface field strength? In later chapters of these notes we will encounter various lines of arguments, both observational and theoretical, indicating that it should increase with increasing rotation rate. Some of the dynamo models we will construct in chapter 10 would "predict" $B_{r0} \propto \Omega$. If this is the case, and for a fixed moment of inertia on the main-sequence (a very good approximation, for a change...), then eq. (5.40) would lead to

$$\frac{\mathrm{d}\Omega}{\mathrm{d}t} \propto \Omega^3 \ , \tag{5.42}$$

which readily integrates to

$$\frac{1}{\Omega^2(t)} - \frac{1}{\Omega^2(t_0)} \propto t - t_0 \ , \tag{5.43}$$

where t_0 is the time of arrival on the ZAMS (or shortly thereabouts). In the asymptotic limit $t \gg t_0$, $\Omega \ll \Omega(t_0)$, this becomes

$$\Omega(t) \propto t^{-1/2} \ , \tag{5.44}$$

which, how about that, is precisely the power-law relationship inferred observationally by Skumanich (cf. Fig. 5.7). Looks like we're in business!

5.3.3 The spindown of late-type stars

The missing proportionality constant in eq. (5.44) is of course readily computed from our Weber-Davis solution; in fact we did nearly all the work already in arriving at eq. (5.41), the missing element being the expression of stellar angular momentum in terms of a star's angular velocity distribution. If, for the time being, we assume that stars rotate as rigid bodies, then we have

$$J = I_* \Omega_* \ , \tag{5.45}$$

and dimensional analysis yields the following expression for the **spin-down timescale**:

$$\tau_{\rm sp} = \frac{1}{I_* \Omega_*} \left(\frac{{\rm d}J}{{\rm d}t} \right)^{-1} \ . \tag{5.46}$$

All we are missing are the stellar moments of inertia, which are readily computed if we have stellar structural models on hand. The third column of Table 5.4 list the resulting spin-down timecales, for ZAMS stellar models between 0.8 and 1.2 $M_\odot$. In all cases it as assumed that the ZAMS rotation period is one day, and the radial surface magnetic field strength is 50 G, reasonable numbers to the extent we can tell from observations and models of stellar formation and pre-main-sequence evolution.

Table 5.4
ZAMS spindown timescales for late-type stars[6]

$M/M_\odot$	$R/R_\odot$	$I_*[10^{53}]$	$\tau_{J,*}$ [Myr]	$I_E[10^{53}]$	$\tau_{J,E}$ [Myr]
0.8	0.703	4.41	810	1.025	188
0.9	0.784	5.50	604	0.979	107
1.0	0.882	6.75	396	0.833	48.9
1.2	1.131	9.02	133	0.139	2.05

The spin-down timescales are of order 10^8 and 10^9 yr, which is nicely smaller than the solar age, but a factor of ten longer than the spin-down timecales inferred from $v \sin i$ determinations in young stellar clusters. Observations do offer an interesting hint, in that after arriving on the main-sequence, more massive stars seem to spin down *faster* than less massive stars, even though their moment of inertia is larger (second column of Table 5.4).

The favored escape from this quandary is to assume that the torque applied by the wind to the photospheric layers is not transmitted throughout the whole star, but (at first anyway) only to its convective envelope, where the vigorous turbulent thermally-driven convective fluid motions are expected to redistribute momentum on the convective turnover time, of the order of a month for convection in solar-type stars. Now, the thickness of the convection decreases

[6]Stellar structural models courtesy of S. Vanderberg, U. Victoria.

rapidly as mass increases, leading to a decrease of the moment of inertia of main-sequence convective envelope with increasing mass (see fifth column in 5.4. This then leads to spin-dowm times (last column in Table 5.4) that (1) are in much better agreement with observationally-inferred values (2) *decrease* with increasing mass. It all fits together!

In late type stars spun down by a wind-mediated surface torque, many physical processes can exchange angular momentum between the convective envelope and underlying radiative core. Indeed, helioseismology has shown that the angular velocity of the solar core is comparable to that of its convective envelope, implying that whatever dynamical coupling is taking place between the core and envelope acts on a timescale much smaller than the solar age (but still significantly longer that the ZAMS spindown timescales, otherwise we're in trouble again). It turns out that internal magnetic fields can do the trick, and remain at this writing the most physically viable explanation for the rotation rate of the solar radiative core. To substantiate this claim would take us too deep inside the sun, but references listed in the bibliography to this chapter provide good entry points into this area of research. Time to get back up into the wind and see what we can do about those famous high-speed streams...

5.4 Wind driving by Alfvén waves

In the solar photosphere, the plasma-β is high enough that magnetic fieldlines get continuously displaced by convective fluid motions. Vertical displacements will generate magnetosonic waves, which are expected to shock and dissipate before they reach the corona. Horizontal displacements of magnetic fieldlines, on the other hand, will propagate upwards into the corona in the form of Alfvén waves. These, it turns out, can have a significant dynamical impact on wind-like outflows, and this is what we'll look into in this section.

The physical/geometrical setup we consider here closely resembles that of the Weber-Davis solution of §5.1, i.e., working in spherical polar coordinates we solve the steady ($\partial/\partial t = 0$) axisymmetric ($\partial/\partial\phi = 0$) wind equations in the equatorial plane of the star, assuming a radial reference magnetic field. The two important differences are: (1) rotation is neglected, and (2) we consider an isothermal, rather than polytropic wind, otherwise the mathematics really get too messy.

The key in formulating the wave-wind model is to assume that the total flow and magnetic field can be written as

$$\mathbf{u}(r,t) = u_r(r)\hat{\mathbf{e}}_r + \delta u(r,t)\hat{\mathbf{e}}_\phi \ , \tag{5.47}$$

$$\mathbf{B}(r,t) = B_r(r)\hat{\mathbf{e}}_r + \delta B(r,t)\hat{\mathbf{e}}_\phi \ , \tag{5.48}$$

where u_r, B_r define the large-scale wind outflow, and the two leftmost terms correspond to a transverse wave travelling in the r-direction and "oscillating" in the ϕ-direction; that latter choice is entirely arbitrary, but will facilitate the mathematical developments to follow. As with any wave, the time averages of the local wave contribution to the flow and field vanish:

$$\langle \delta u \rangle = 0 \ , \qquad \langle \delta B \rangle = 0 \ . \tag{5.49}$$

5.4.1 The magnetic force exerted by Alfvén waves

Looking at the momentum equation, you should be able to convince yourself that the contribution to the r-component of the force per unit volume (f_w) associated with the wave is given by:

$$f_w = \left(\rho(\delta\mathbf{u}\cdot\nabla)\delta\mathbf{u} + \frac{1}{\mu_0}(\nabla\times\delta\mathbf{B})\times\delta\mathbf{B} \right)_r \ . \tag{5.50}$$

For the assumptions embodied in eqs. (5.47)–(5.49), time averaging of this expression over a wave period yields

$$\langle f_w \rangle = \frac{\rho \langle \delta u^2 \rangle}{r} - \frac{\langle \delta B^2 \rangle}{\mu_0 r} - \frac{\mathrm{d}}{\mathrm{d}r}\left(\frac{\langle \delta B^2 \rangle}{2\mu_0} \right) \ . \tag{5.51}$$

There are thus two contribution to the wave-induced force: a centrifugal force associated with the wave displacement in the ϕ-direction (first term on RHS of eq. (5.51), and a Lorentz force that can be broken into tension and magnetic pressure gradient contributions[7].

But how to we compute δu and δB? Simply by solving the ϕ-components of the momentum and induction equations, which here reduce to

$$\frac{\partial}{\partial t}\delta u_r + \frac{u}{r}\frac{\partial}{\partial r}(r\delta u) = \frac{B_r}{\mu_0 \rho r}\frac{\partial}{\partial r}(r\delta B) \ , \tag{5.52}$$

$$\frac{\partial}{\partial t}\delta B = \frac{1}{r}\frac{\partial}{\partial r}\left(r(B_r \delta u - u_r \delta B)\right) \ , \tag{5.53}$$

with B_r and u_r given by the "wind" part of the governing equation; these take on the usual form for a steady, spherically-symmetric outflow (cf. §3.3), except that now the isothermality assumption leads to

$$u_r \frac{\mathrm{d}u_r}{\mathrm{d}r} = -\frac{a^2}{r} - \frac{GM}{r^2} + \frac{\langle f_w \rangle}{\rho} \ , \tag{5.54}$$

where $a = \sqrt{kT/m}$ is the **isothermal sound speed** for a perfect gas. As in the Weber-Davis case, the constraints of mass and magnetic flux conservation lead to

$$\frac{\rho(r)}{\rho_0} = \left(\frac{r_0}{r}\right)^2 \left(\frac{u_{r0}}{u_r}\right) \ , \tag{5.55}$$

$$\frac{B_r(r)}{B_{r0}} = \left(\frac{r_0}{r}\right)^2 \ . \tag{5.56}$$

So, in principle all is well: with $B_r(r)$ known from (5.56) and provided all needed physical quantities are specified at the coronal base r_0, we have here a set of four coupled equations (namely (5.52), (5.53), (5.54), and (5.55)) for the four unknown functionals u_r, ρ, δu and δB. However, the strong nonlinear coupling mediated by eq. (5.51) is not easy to deal with in general, so we need to introduce an additional approximation into the model.

5.4.2 The Wave force in the WKB approximation

The heart of the so-called WKB approximation is to assume that the wavelength λ of the propagating Alfvén wave is much smaller than the length scale ℓ over which the background flow is varying. In such cases one can expand the wave amplitudes δu and δB as

$$\delta u(r,t) = \left[\delta u_1(r) + \epsilon \delta u_2(r) + \epsilon^2 \delta u_3(r) + ...\right] \exp(i[\psi(r) - \omega t]) \tag{5.57}$$

with a similar expression characterizing δB, $\varepsilon = \lambda/\ell = 2\pi/k\ell$ is a small parameter, and $k(r) = \mathrm{d}\psi/\mathrm{d}r$ is the radius-dependent wavenumber. Inserting these expression into eqs. (5.52)—(5.53), one then equates all terms of similar power in ϵ. To lowest order this yields

$$\omega = k(u_r + A_r) \ , \tag{5.58}$$

[7] As you get to verify in problem 5.1 below, the spherical geometry is essential here in producing a non-zero time-averaged wave force.

$$\delta u_1 = \pm \frac{\delta B}{\sqrt{4\pi\rho}} \ , \tag{5.59}$$

with the minus sign retained in what follows, since it corresponds to the outward propagating waves. Substituting these expression in the first order equations leads to a differential equation for δB_1, which (it can be shown...) integrates to

$$\delta B(r) = \delta B_0 \left(\frac{M_{A0}}{M_A}\right)^{1/2} \left(\frac{1+M_{A0}}{1+M_A}\right)^{1/2} \ , \tag{5.60}$$

where

$$M_A \equiv \frac{u_r}{A_r} = M_{A0} \left(\frac{\rho_0}{\rho}\right)^{1/2} \tag{5.61}$$

is the **Alfvénic Mach Number**, the Alfvén speed A_r here being the component associated with the radial magnetic field component, and the subscript "1" has been dropped for clarity. The corresponding expression for $\delta u(r)$ follows directly from eq. (5.59). Substituting all this back into eq. (5.51) for the time-averaged wave force, one eventually arrives at

$$\langle f_w \rangle = -\frac{\mathrm{d}}{\mathrm{d}r}\left(\frac{\langle \delta B^2 \rangle}{8\pi}\right) = \frac{\langle \epsilon_w \rangle}{4}\left(\frac{1+3M_A}{1+M_A}\right)\left(\frac{2}{r} + \frac{1}{u_r}\frac{\mathrm{d}u_r}{\mathrm{d}r}\right) \tag{5.62}$$

where

$$\langle \epsilon_w \rangle = \frac{\langle \delta B^2 \rangle}{4\pi} = \frac{\langle \delta B_0^2 \rangle}{4\pi}\left(\frac{M_{A0}}{M_A}\right)\left(\frac{1+M_{A0}}{1+M_A}\right)^2 \tag{5.63}$$

is the wave energy density. The RHS of eqs. (5.62)—(5.63) now involve only properties of the large-scale outflow, so in principle we can proceed with confidence.

5.4.3 Obtaining wind solutions

Getting a complete wind solution once again is done numerically. Substituting the expression for the wave force obtained above into the r-component of the momentum equation (5.54) leads, after a fair bit of algebraic juggling, to

$$\left[u_r^2 - a^2 - \frac{\langle \epsilon_w \rangle}{4\rho}\left(\frac{1+3M_A}{1+M_A}\right)\right]\frac{r}{u_r}\frac{\mathrm{d}u_r}{\mathrm{d}r} = \left[a^2 - \frac{GM}{r} + \frac{\langle \epsilon_w \rangle}{2\rho}\left(\frac{1+3M_A}{1+M_A}\right)\right] \ . \tag{5.64}$$

This imposing equation is best treated as a initial value problem for u_r, of the general form:

$$\frac{\mathrm{d}u_r}{\mathrm{d}r} = g(r) \ . \tag{5.65}$$

Assuming a starting guess for the base flow speed u_{r0} (for example that of the pure isothermal solution), eq. (5.64) is integrated forward in r using some suitable ODE integration scheme (see Appendix **??**). The problem is that the solution must go through a sonic critical point. If the starting guess is wrong, as one integrates forward in r there will come a point where the solution will diverge (infinite acceleration). The starting guess must then be adjusted upwards or downwards depending on how divergence occurs, and the process repeated until one finds a solution that shoots smoothly through the critical point and sails away ever on and on until you reach a value of r that is a good enough approximation of infinity for practical purpose (we'll settle for $100\,r_0$ in what follows). Then it is a simple matter to reconstruct ρ via eq. (5.55), then δB via (5.60), and finally δu via (5.59).

5.4.4 Some representative solar solutions

We first consider the effect of Alfvén wave driving on solar-type outflows. Accordingly, the reference parameters for our reference isothermal solution (without waves) are chosen to produce wind characteristics at 1AU commensurate with low-speed streams; we thus set $T_0 = 10^6\,K$ leading to an isothermal sound speed $a = 129\,\mathrm{km\ s^{-1}}$ and $N = 2\times10^{13}\,\mathrm{cm^{-3}}$. This flow has a base speed $u_{r0} = 1.19\,\mathrm{km\ s^{-1}}$ becomes supersonic at $r_s/r_0 = 4.6$, and reaches $\simeq 450\,\mathrm{km\ s^{-1}}$ at 1AU. We set the base radial magnetic field at $B_{r0} = 10^{-4}\,\mathrm{T}$, and set the size of the magnetic pertubation at the base via the parameter

$$\alpha = \left(\frac{\delta B_0}{B_0}\right)^2 \ , \tag{5.66}$$

measuring the base ratio of magnetic energy density in the wave to that in the background magnetic field.

Wind profiles are shown on Fig. 5.8 for three values of the parameter α, with the corresponding profiles of wave amplitudes plotted on Fig. 5.9. Several features of these wind solutions are noteworthy. The wind speed is an increasing function of Alfvén wave amplitude (not surprisingly), but the increase is proportionaly greater at the base of the wind (from $4.85\mathrm{km\,s^{-1}}$ at $\alpha = 0.01$ up to $37.35\mathrm{km\,s^{-1}}$ at $\alpha = 0.1$) as compared to the wind speeds at large distances (from $888\mathrm{km\,s^{-1}}$ to $1005\mathrm{km\,s^{-1}}$ at $100\,r_0$). As mentioned in the preceding chapter, this behavior is characteristic of situations where additional momentum occurs primarily within the sonic point, located at $r_A/r_0 = 13.53$, 8.54 and 4.85 for $\alpha = 0.01$, 0.03 and 0.1, respectively. The wave amplitude decrease rapidly with distance, reflecting the $1/r^2$ behavior of B_r but also the fact that wave energy is being transfered to the wind. The increase of $\langle \delta u^2 \rangle$ in the first ten r_0 or so is a direct reflection of the rapid decrease of the density with r. This causes the inertia of the fluid to decrease faster than the wave's restoring force, leading to an increase in $\langle \delta u^2 \rangle$ even though $\langle \delta B^2 \rangle$ falls off rapidly (cf. eq. 5.59). Indeed it can be easily shown that in the sub-Alfvénic portion of the wind the wave amplitude scale as $\langle \delta u^2 \rangle^{1/2} \sim \rho^{1/4}$ and $\langle \delta B^2 \rangle^{1/2} \sim \rho^{-1/4}$ while in the superAlfvénic portion of the wind, where the Alfv'én speed is nearly constant, the amplitudes scale as $\langle \delta u^2 \rangle^{1/2} \sim r^{-1/2}$ and $\langle \delta B^2 \rangle^{1/2} \sim r^{-3/2}$.

Figure 5.10 depicts details of the force balance in the $\alpha = 0.01$ and 0.1 solutions. As with the Parker wind solution considered in §3.3, near the base the flow is in near-hydrostatic equilibrium, with the Alfvén wave force contributing little even at $\alpha = 0.1$. However the wave force rapidly starts to dominate the dynamics at larger distances, exceeding the thermal pressure force beyond the Alfvén point.

You shouldn't be too impressed by the $\sim 1000\,\mathrm{km\ s^{-1}}$ asymptotic speeds of our wave-enhanced wind solutions. Even though this is largely sufficient to account for high-speed streams, in fact the isothermality assumptions guarantees that the asymptotic flow speed tends to... infinity! (Haven't you done Problem 3.7 already?). What *is* noteworthy is that beyond the sonic point, the wind solution with WKB Alfvén waves has a flow speed a factor of about two larger than the reference wave-free isothermal solution, which *is* the speedup factor suggested by Table 3.1. And this results, it turns out, does carry over to polytropic version of the model.

5.4.5 Wave-driven winds

There many classes of non-solar late-type stars that show evidence for wind-like outflows, most notably giants and supergiants of spectral type K and later, yet their inferred coronal temperatures are too low for sustaining a (mostly) thermally-driven wind. Wind acceleration via collisional coupling to dust grains propelled by radiative pressure is a possibility, but the efficiency of this mechanism depends a lot on the details of grain formation and coupling to the gas; at the present time this appears a viable mechanism only for the coolest supergiants. With all but the coolest of these stars showing evidence for magnetic activity, wind driving through energy deposition by MHD waves is certainly another option. Dissipation of acoustic and magnetoacoustic waves has been shown able to produce chromospheric-type heating, but

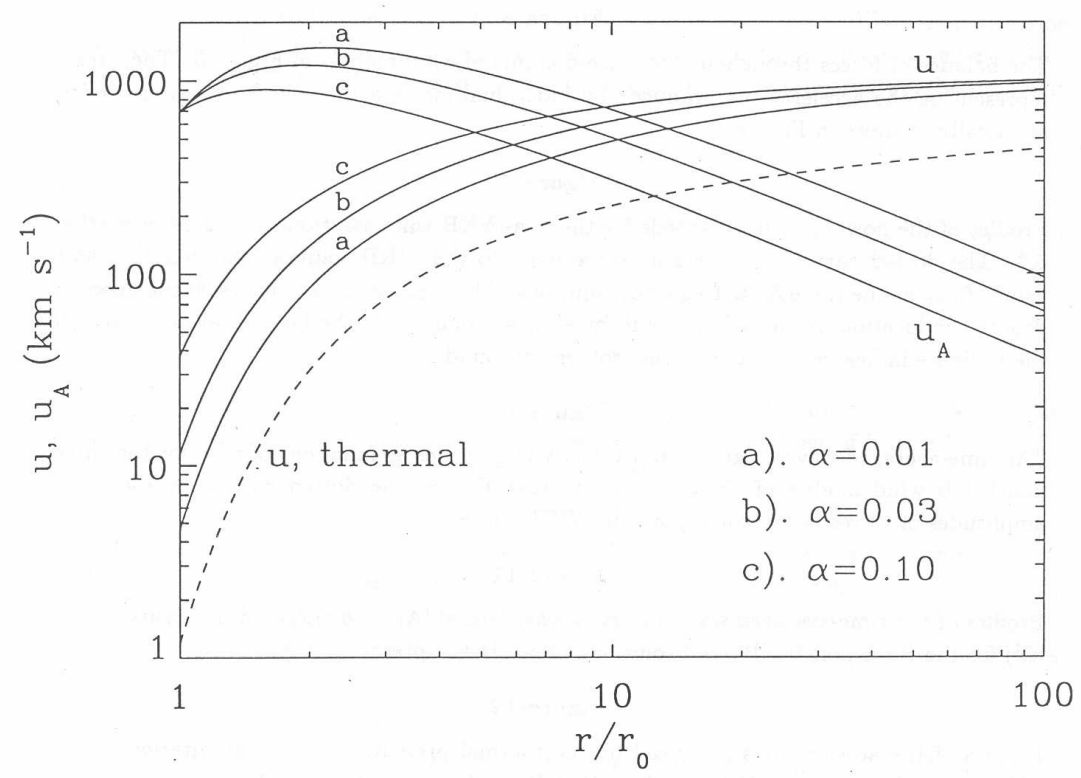

Figure 5.8: Radial profiles of the flow and Alfvén speed (here denoted u_A) for wave-driven isothermal wind models in the WKB approximation. The three solutions depicted here are obtained for three distinct values of the forcing amplitude parameter $\alpha = (\delta B_0/B_0)^2$, as labeled. The dashed curve is the flow profile for an equivalent isothermal solution without any wave driving. Reproduced from the MacGregor & Charbonneau 1994 book chapter cited in the bibliography.

in itself most probably cannot drive substantial winds. This pretty much leaves Alfvén wave driving as the most promising candidate. The references given the bibliography should provide good entry points in this vast literature.

All the results discussed so far are predicated on the use of the WKD approximation in computing the force exterted by the Alfvén waves on the flow. This is expected to be a good approximation provided the wave period is much shorter than the advective transit time on the wind over a distance over which background properties of the flow (in particular the Alfvén speed) vary significantly. For the solar-type solutions considered in §5.4.4, it can be verified that waves with periods larger than about 10 minutes will violate the WKB constraints near the base of the flow, where the gradient in Alfvén speed is substantial (cf. Fig. 5.8). Now, ten minutes is about the turnover time for solar photospheric granules, so wave power in this period range may well be significant. It turns out that relaxing the WKB approximation has little impact on solar-type solutions, but large differences do materialize in wind models where the wave force is the primarily driver. If you wish to look deeper into this aspect of the problem, see the references listed in the bibliography to this section.

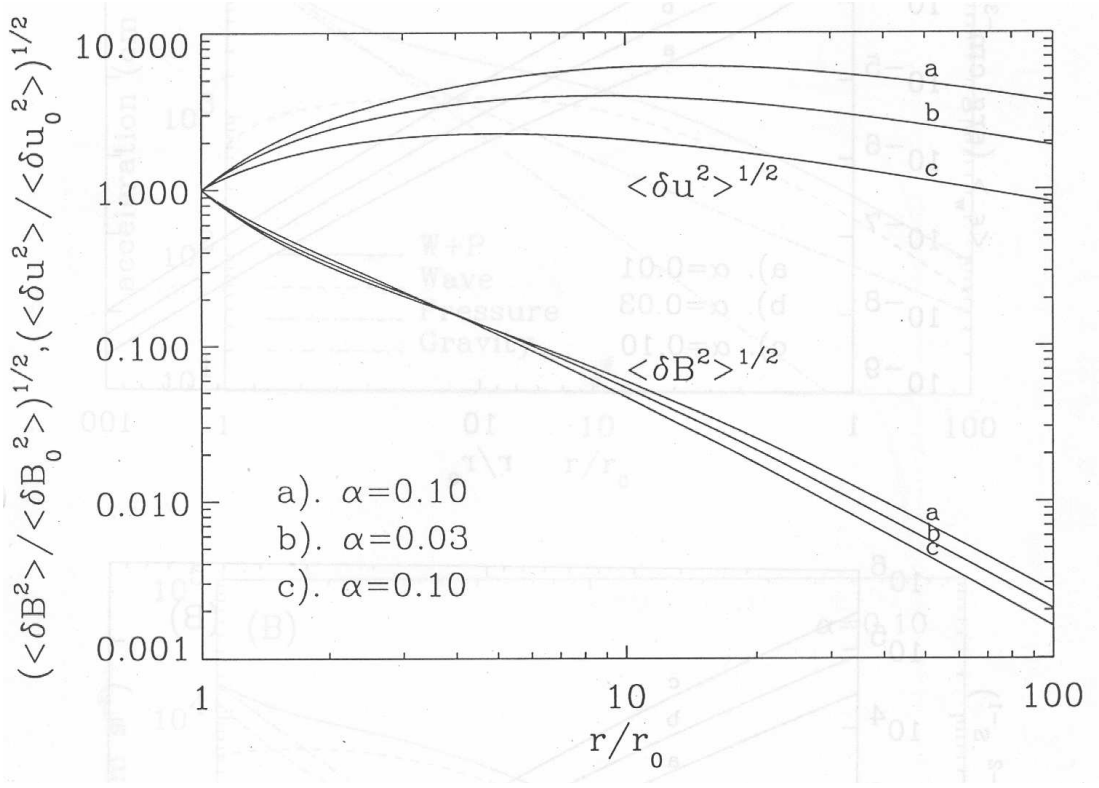

Figure 5.9: Time averaged wave velocity and magnetic amplitudes as a function of r/r_0, for the solutions of Fig. 5.8. In all cases amplitudes are normalized to their value at the reference radius r_0 On each panel the solid curve is the sum of the wave and thermal pressure gradient accelerations. Reproduced from the MacGregor & Charbonneau 1994 book chapter cited in the bibliography.

Problems:

1. Repeat the derivation of $\langle f_w \rangle$ for a homogeneous cartesian flow, i.e., set

$$\mathbf{u}(x,t) = u_0 \hat{\mathbf{e}}_x + \delta u(x,t) \hat{\mathbf{e}}_z \ ,$$
$$\mathbf{B}(x,t) = B_0 \hat{\mathbf{e}}_x + \delta B(x,t) \hat{\mathbf{e}}_z \ .$$

2. Work out the missing mathematical steps leading to eq. (5.19).

3. Make the (bold) assumption that the Weber-Davis solution obtained in §5.1 remains valid outside of the equatorial plane. Demonstrate that if this is the case, there exists an unbalanced force term in the θ-component of the momentum equation. Discuss in qualitative terms (not actual calculations, unless you're really an eager beaver...) how the wind solution would be altered.

4. Assuming that stars arrive on the zero-age main-sequence in state of solid-body rotation, calculate their subsequent rotational evolution on the main-sequence. Plot Ω as a function of time, for stars of 0.8 and 1.2 $M_\odot$, and ZAMS rotation rates of 200, 100, 50 and 10 $\mathrm{km\,s^{-1}}$, under the following two assumptions regarding internal angular momentum disrtibution:

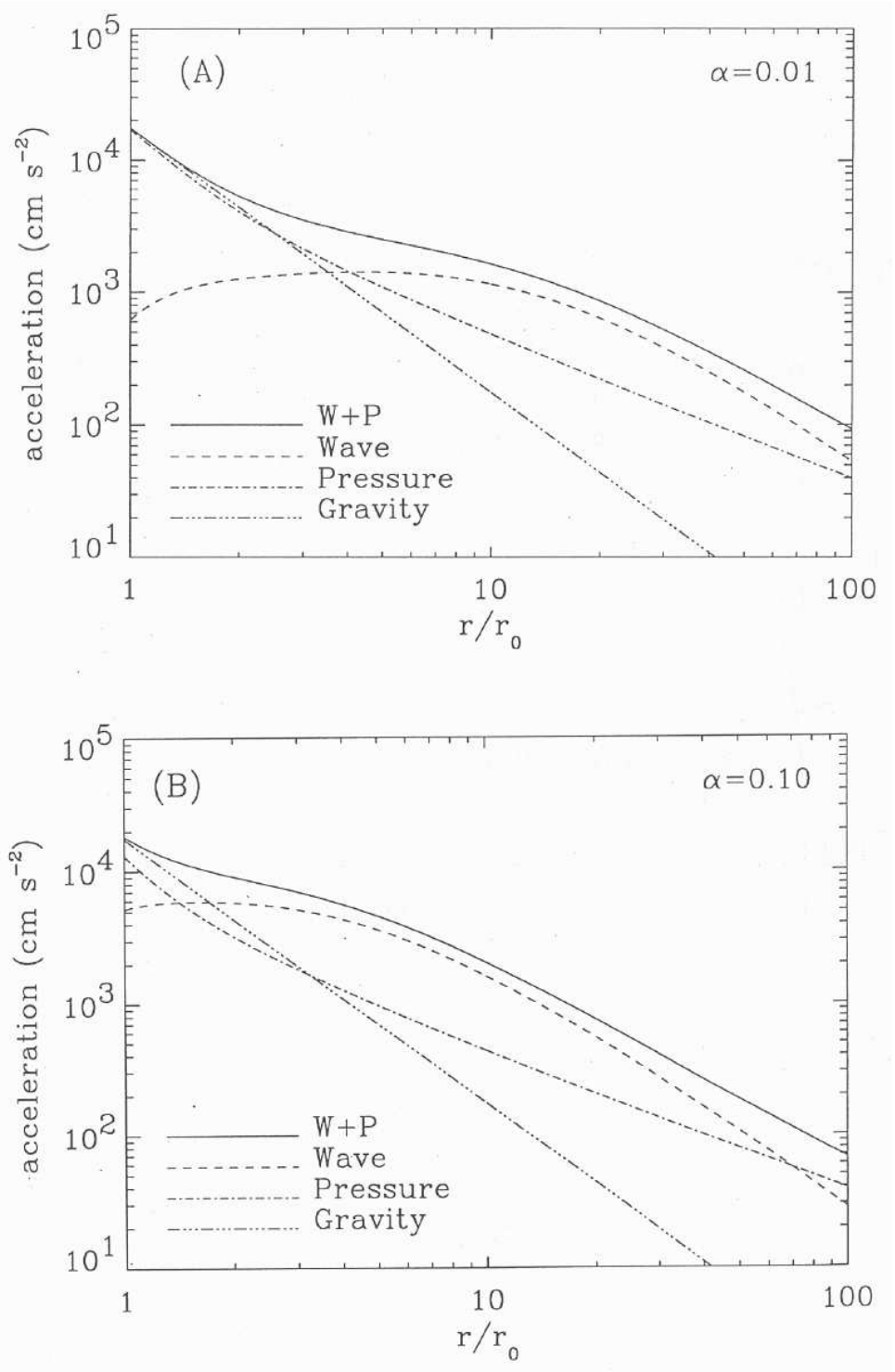

Figure 5.10: Force balance in the (A) $\alpha = 0.01$ and (B) $\alpha = 0.1$ solutions of Figs. 5.8–5.9. On each panel the solid curve is the sum of the wave and thermal pressure gradient accelerations. Reproduced from the MacGregor & Charbonneau 1994 book chapter cited in the bibliography.

(a) The stars rotate as rigid bodies throughout main-sequence evolution

(b) Only the outer convective envelope is spun-down by the wind-mediated torque.

Your starting point is eq. (5.41), with the additional "dynamo" assumption $B_{r0} \propto \Omega$ already encountered in deriving Skumanich's square root law, and the moment of inertia data listed in Table 5.4. How does the assumption made regarding internal angular momentum redistribution affect the spreads in rotation rates at age 100Myr? 1Gyr?

5. Work out the missing mathematical steps leading to eq. (5.64).

Bibliography:

The original MHD wind paper by Weber and Davis is

Weber, E.J., & Davis, L. Jr. 1967, ApJ, 148, 217.

but the presentation of §5.1 follows mostly

Belcher, J.W., & MacGregor, K.B. 1976, ApJ, 210, 498.

The confrontation of the WD wind model with the observed solar wind is discussed critically in

Pizzo, V., Schwenn, R., Marsch, E., Rosenbauer, H., Mülhaüser, K.-H., & Neubauer, F.M. 1983, ApJ, 271, 335.

If you are interested in application of the WD model to protostars or hot stars, see respectively:

Hartmann, L., & MacGregor, K.B. 1982, ApJ, 259, 180.
Friend, D.B., & MacGregor, K.B. 1984, ApJ, 282, 591.

The following are a small selection of noteworthy (very) early papers on stellar rotation, including those alluded to in §5.3.1:

Vogel, H.C. 1872, Astron. Nachr., 78, 248,
Abney, W. de W. 1877, MNRAS, 37, 278,
Schlesinger, F. 1909, Pub. Allegheny Obs., 1, 123,
Elvey, C.T. 1929, ApJ 70, 141.

The idea that magnetized outflows can lead to stellar angular momentum loss can be traced to

Schatzman, E. 1962, Ann. Astrophys., 25, 18.

In this context, another important early paper is

Mestel, L. 1968, MNRAS, 138, 359.

The first theoretical derivation of Skumanich's square root relation in the context of $\alpha\Omega$ dynamo theory is due to

Durney, B. 1972, in *Solar Wind*, eds. C.P. Sonett, P.J. Coleman, & L.M. Wilcox (Washington: NASA), p. 282.

There is a huge literature out there on the rotational evolution of late-type stars on or near the main-sequence; on the observational front, including the case for core-envelope decoupling, see:

Stauffer, J.R., & Hartmann, L.W. 1986, ApJ, 318, 337,
Soderblom, D.R., Stauffer, J.R., MacGregor, K.B., & Jones, B.F. 1993, ApJ, 409, 624,
A recent review?

while a good feel for the range of modelling approaches, assumptions (and debates!) can be obtained from taking a look at

MacGregor, K.B., & Brenner, M. 1991, ApJ, 376, 204,
Charbonneau, P., & MacGregor, K.B. 1993, ApJ, 417, 762,
Chaboyer, B., Demarque, P., & Pinsonneault, M. 1995, ApJ, 441, 865,
Keppens, R., MacGregor, K.B., & Charbonneau, P. 1995, A&A, 294, 469,
Charbonnel, C., & Talon, S. 2005, Science, 309(7544), 2189.

The content of §5.2 is largely based on the following two papers:

Keppens, R., & Goedbloed, J.P. 1999, *Astron. Astrophys.*, **343**, 251-260,
Keppens, R., & Goedbloed, J.P. 2000, *Astrophys. J.*, **530**, 1036-1048,

The content of section 5.4 is, to a large extent, adapted from the following book chapter:

MacGregor, K.B., & Charbonneau, P. 1994, in *Cosmic winds and the heliosphere*, ed. J.R. Jokipii, C.P. Sonett, & M.S. Giampapa, Tucson: University of Arizone Press, 327-ff.

with Figures 5.8, 5.9 and 5.9 in fact digitized straight out of these pages. The many "it can be shown" in §5.4.2, implicit or explicit, are substantiated in

Belcher, J.W. 1971, ApJ, 168, 509,
Hollweg, J.V. 1973, JGR, 78, 3643.

On the non-WKB generalization of these models, see

MacGregor, K.B., & Charbonneau, P. 1994, ApJ, 430, 387,
Charbonneau, P., & MacGregor, K.B. 1995, ApJ, 454, 901,

and references therein. On the observational front, a very recent and spectacular breakthrough is the direct observation of Alfvén waves in the solar corona; see

Tomczyk, S., McIntosh, S.W., Keil, S.L., Judge, P.G., Schad, T., Seeley, D.H., Edmonson, J. 2007, Science, **317**(5842), 1192.

On numerical MHD simulations of wind driving by Afvén waves, see, e.g.

Suzuki, T.K., & Inutsuka, S. 2006, JGR, 111(A6), A06101,

and references therein. On wind driving by acoustic and magnetosonic waves in cool, evolved stars, see, e.g.,

Hartmann, L., & MacGregor, K.B. 1980, ApJ, 242, 260,
Cuntz, M. 1990, ApJ, 353, 255,

and the Lamers & Cassinelli book listed in the bibliography to chapter 3.